Supporting Information

Multi-atomic Loaded C_2N_1 Catalysts for CO_2 Reduction to CO or Formic Acid

Yimeng Sun [a], Lin Tao [a, *], Mingjie Wu [b, *], Davoud Dastan [c],

Javed Rehman [d], Lixiang Li [a], and Baigang An [a, *]

[a] *School of Chemical Engineering, University of Science and Technology Liaoning, Anshan 114051, China*

[b] *State Key Laboratory of New Textile Materials and Advanced Processing Technologies, Wuhan Textile University, Wuhan 430200, China*

[c] *Department of Materials Science and Engineering, Cornell University, Ithaca, NY 14850, United States*

[d] *State Key Laboratory of Metastable Materials Science and Technology, Yanshan University, Qinhuangdao 066004, China*

*Corresponding authors at:

School of Chemical Engineering, University of Science and Technology Liaoning, Anshan 114051, China

E-mail addresses: **taolin@ustl.edu.cn** (L. Tao),

E-mail addresses: **bgan@ustl.edu.cn** (B. An)

State Key Laboratory of New Textile Materials and Advanced Processing Technologies, Wuhan Textile University, Wuhan 430200, China

E-mail addresses: **mjwu@wtu.edu.cn** (M. Wu)

Contents

Table S1. The adsorption energies (E_{ads}), bond lengths of C and O atoms in CO_2 (d_{c-o}).

O-C-O angles of the most stable CO_2 adsorption configurations on TM-C_2N_1.

Table S2. The adsorption energy of H_2O on the TM-C_2N_1.

Table S3. Diffusion coefficient of CO_2 on TM-C_2N_1.

References

Computational methods

Based on density functional theory (DFT) with periodic boundary conditions, all tasks in this work are calculated in Dmol^3 code [1, 2]. In the calculation process, C-$2s^2 2p^2$, N-$2s^2 2p^3$, O-$2s^2 2p^4$, H-$1s^1$, and Mn-$3d^6 4s^1$, Mo-$4d^5 5s^1$, Ru-$4d^7 5s^1$, Ti-$3d^3 4s^1$ electron orbitals are used as valence electrons, and the interaction between valence electrons and core electrons is described by projector augmented wave method, and generalized gradient approximation The Perdew-Burke-Ernzerhof functional, gradient approximation method correlation describes the exchange association function [3]. To make the result of the total energy more precise, spin polarization is turned on in the calculation and DFT correction is applied. The convergence criteria for energy and force are 10^{-4} eV and 0.05 eV/Å, respectively. When the structure is optimized, the K space is meshed $3 \times 3 \times 1$ with gamma-centered. During the calculation, all atoms in the structure are relaxed.

Catalytic performance calculation method

The computational hydrogen electrode (CHE) model [4, 5] was used to calculate the electrochemical potential of proton-electron pairs and hydrogen under standard conditions:

$$H^+(aq) + e^- \leftrightarrow 1/2H_2 \tag{1}$$

According to this method, the Gibbs free energy change value for each basic reaction is calculated as follows [6]:

$$\Delta G = \Delta E + \Delta E_{ZPE} - T\Delta S \tag{2}$$

Among them, ΔE is the energy difference calculated by DFT, ΔE_{ZPE} is the change in zero-point energy, T is the temperature (298.15 K), and ΔS is the change in entropy. The adsorption energy can determine the stability of CO_2 adsorption on the surface of the catalyst. The adsorption energy formula is as follows [6]:

$$\Delta E_{ads} = E_{system} - \left(E_{surf} + E_{CO_2}\right) \tag{3}$$

where E_{system} is the total energy, E_{surf} and E_{CO2} represent the energy of the surface model and the molecule, respectively. In general, the adsorption energy is negative, indicating that the adsorption process is an exothermic reaction and the adsorption system is stable.

Mechanism analysis calculation details

The mechanism of CO_2 adsorption on the surface of the catalyst can be elaborated by the d-band center theory, and the formula for calculating the d-band center is as follows [7]:

$$\varepsilon_d = \frac{\int_{-\infty}^{\infty} n_d(\varepsilon)\varepsilon d\varepsilon}{\int_{-\infty}^{\infty} n_d(\varepsilon)\varepsilon d\varepsilon} \tag{4}$$

where $n_d(\varepsilon)$ is the density of electrons on the corresponding d band and ε is the energy. In addition, the limiting potential (U_L) is the minimum negative potential that enables heat release for each fundamental step. The formula is

$$U_L = -\Delta G_{max}/e \tag{5}$$

where ΔG_{max} is the maximum value of the change in free energy over the entire CO_2RR path, and e is the amount of electron power [8].

Details of diffusion performance calculation

All MD simulations were carried in a constant number, a constant volume and a constant temperature (NVT) ensemble. The temperature was controlled by using the Nose thermostat. The initial velocity of gas molecules was identical to Boltzmann distribution according to the assumption that the time average is equivalent to the ensemble average. Each MD simulation had a calculation process of 5×10^5 steps. The time step and total simulation time were set to 10 fs and 5 ns, respectively. The first 2 ns was used for equilibration and the last 3 ns of the MD simulation was used for data analysis. Full trajectory was recorded and the frames were output every 500 steps. The diffusion activation energy can be obtained by calculating the gas motion parameters according to molecular dynamics simulation based on our previous work [9], and by this means, the diffusion of CO_2 on a $TM-C_2N_1$ surface can be well verified. Therefore, the mean-squared displacement (MSD) and diffusion coefficients (Ds) were used to investigate the diffusion properties of gases according to the Einstein diffusion law [10], these quantities were computed by the following equations:

$$MSD(t) = \frac{1}{N} \sum_{i=1}^{N} \left\langle \left| r_i(t) - r_i(0) \right|^2 \right\rangle \tag{6}$$

$$D_S = \frac{1}{6} \lim_{t \to \infty} \frac{d}{dt} \sum_{i}^{n} \left\langle \left| r_i(t) - r_i(0) \right|^2 \right\rangle \tag{7}$$

where N is the number of molecules, $r_i(t)$ is the position of molecule when the time is t, and $r_i(0)$ is the initial position.
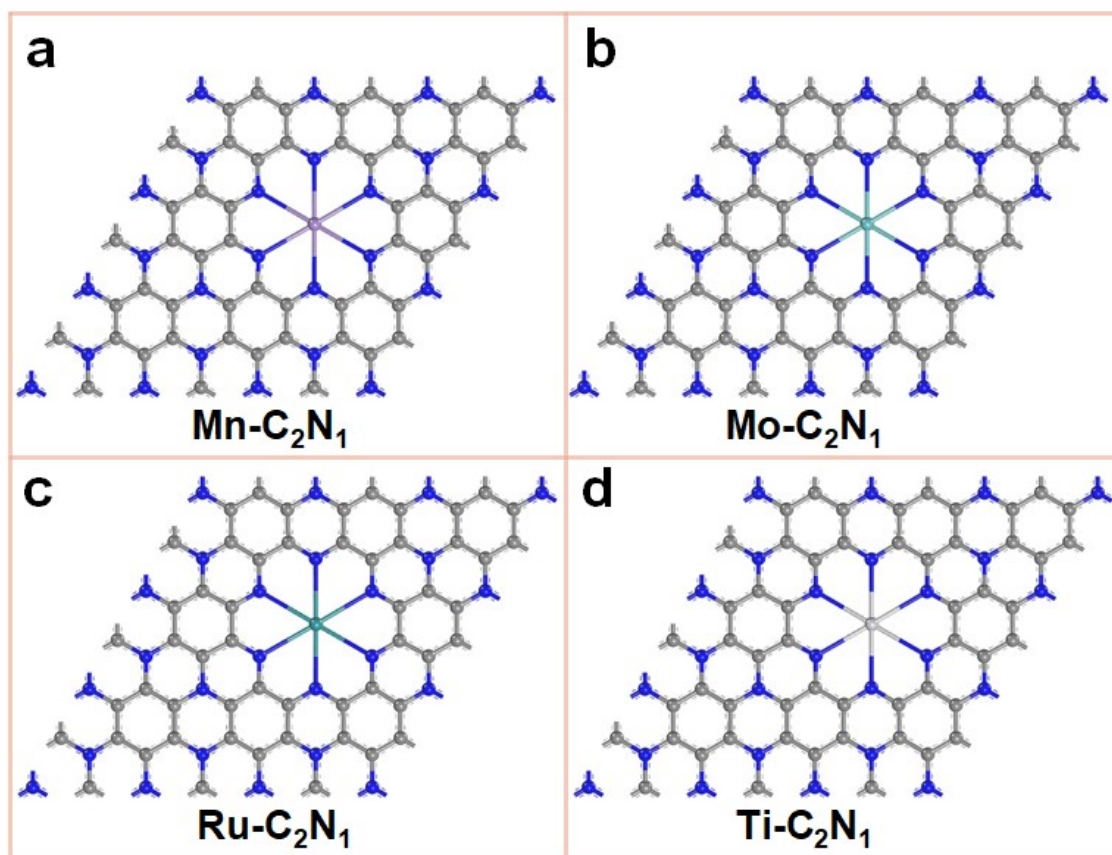
Figure S1. Optimized structure of 1TM-C_2N_1. (a) Mn-C_2N_1. (b) Mo-C_2N_1. (c) Ru-C_2N_1. (d) Ti-C_2N_1.
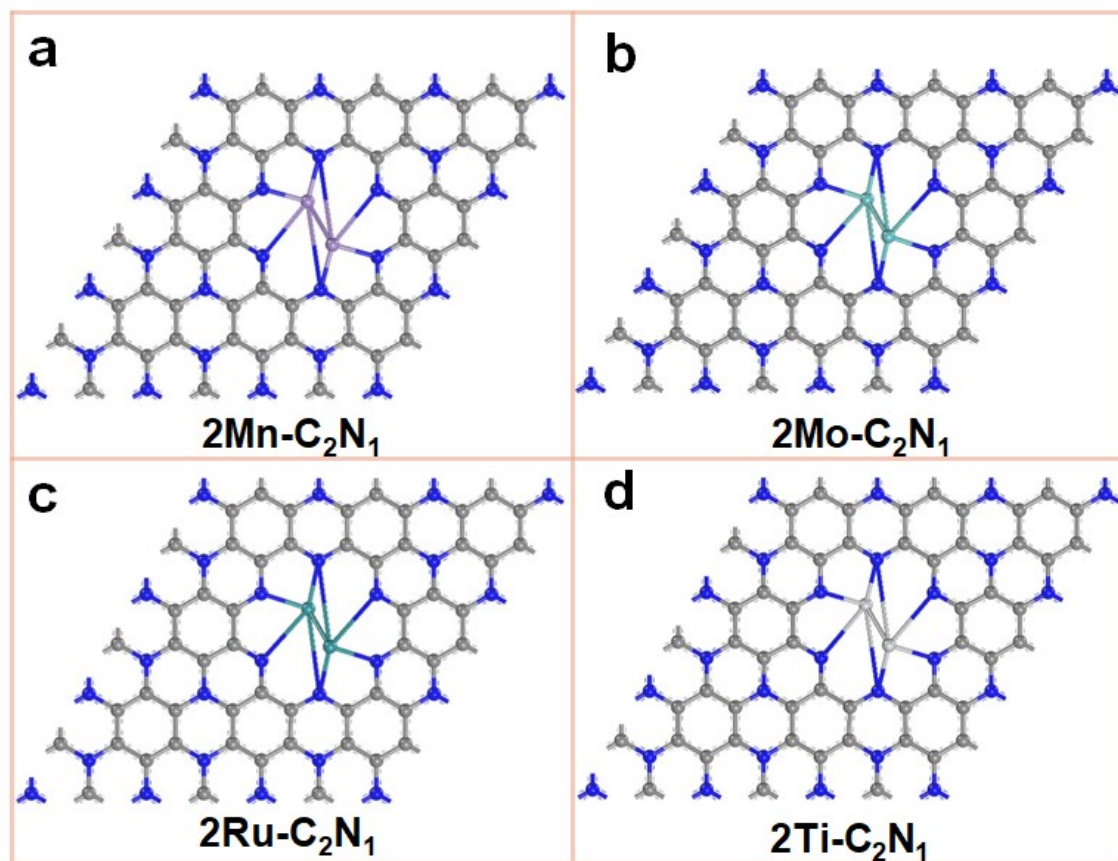
Figure S2. Optimized structure of 2TM-C_2N_1. (a) 2Mn-C_2N_1. (b) 2Mo-C_2N_1. (c) 2Ru-C_2N_1. (d) 2Ti-C_2N_1.
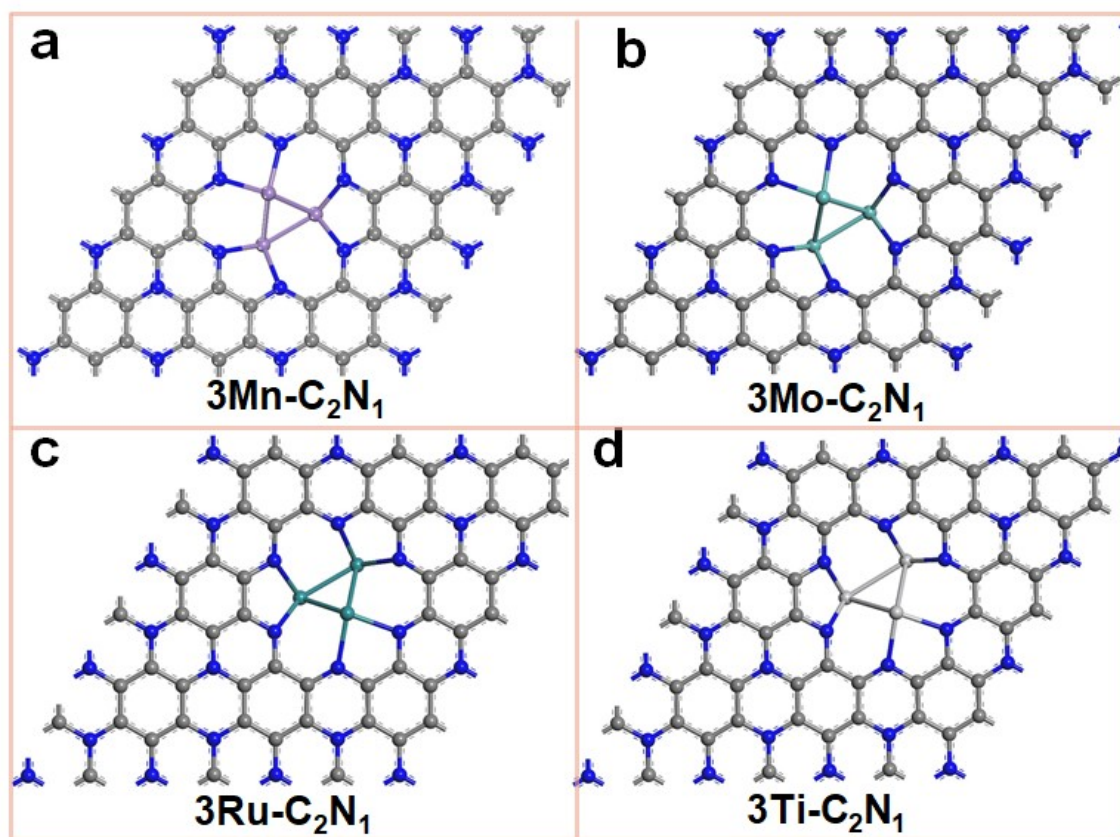
Figure S3. Optimized structure of 3TM-C_2N_1. (a) 3Mn-C_2N_1. (b) 3Mo-C_2N_1. (c) 3Ru-C_2N_1. (d) 3Ti-C_2N_1.
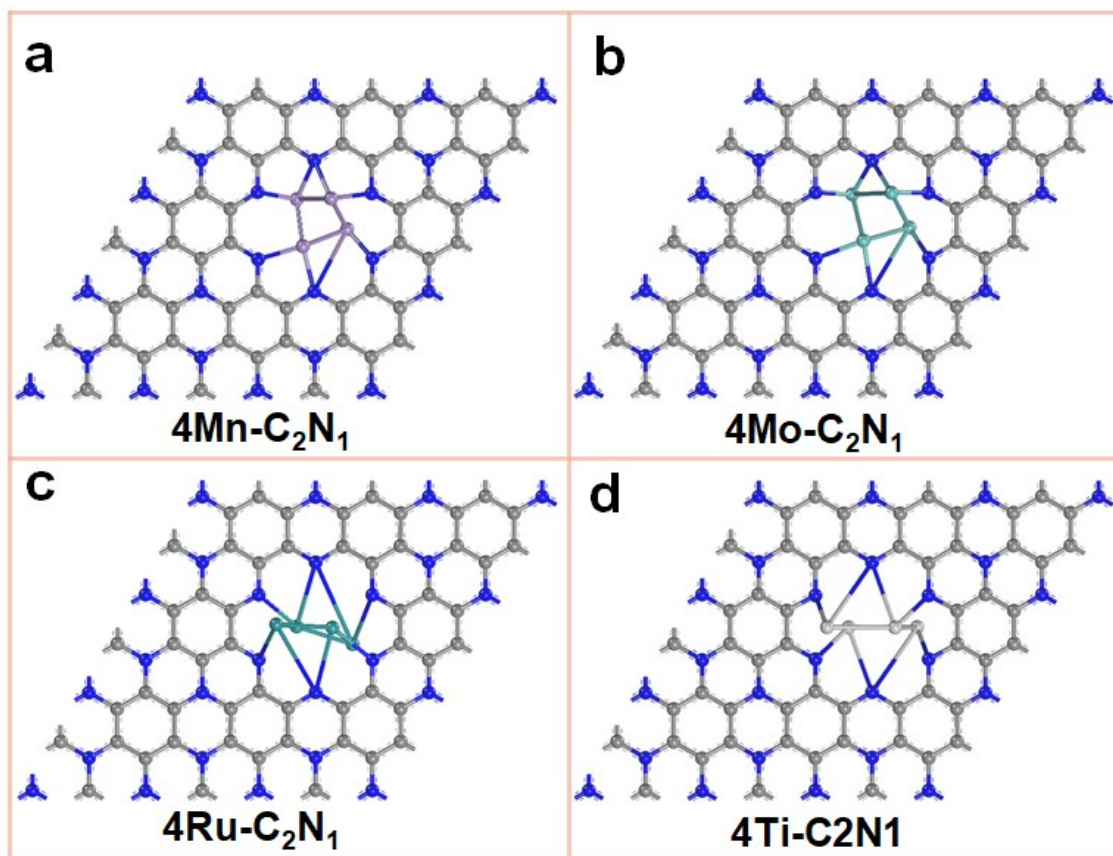
Figure S4. Optimized structure of 4TM-C_2N_1. (a) 4Mn-C_2N_1. (b) 4Mo-C_2N_1. (c) 4Ru-C_2N_1. (d) 4Ti-C_2N_1.
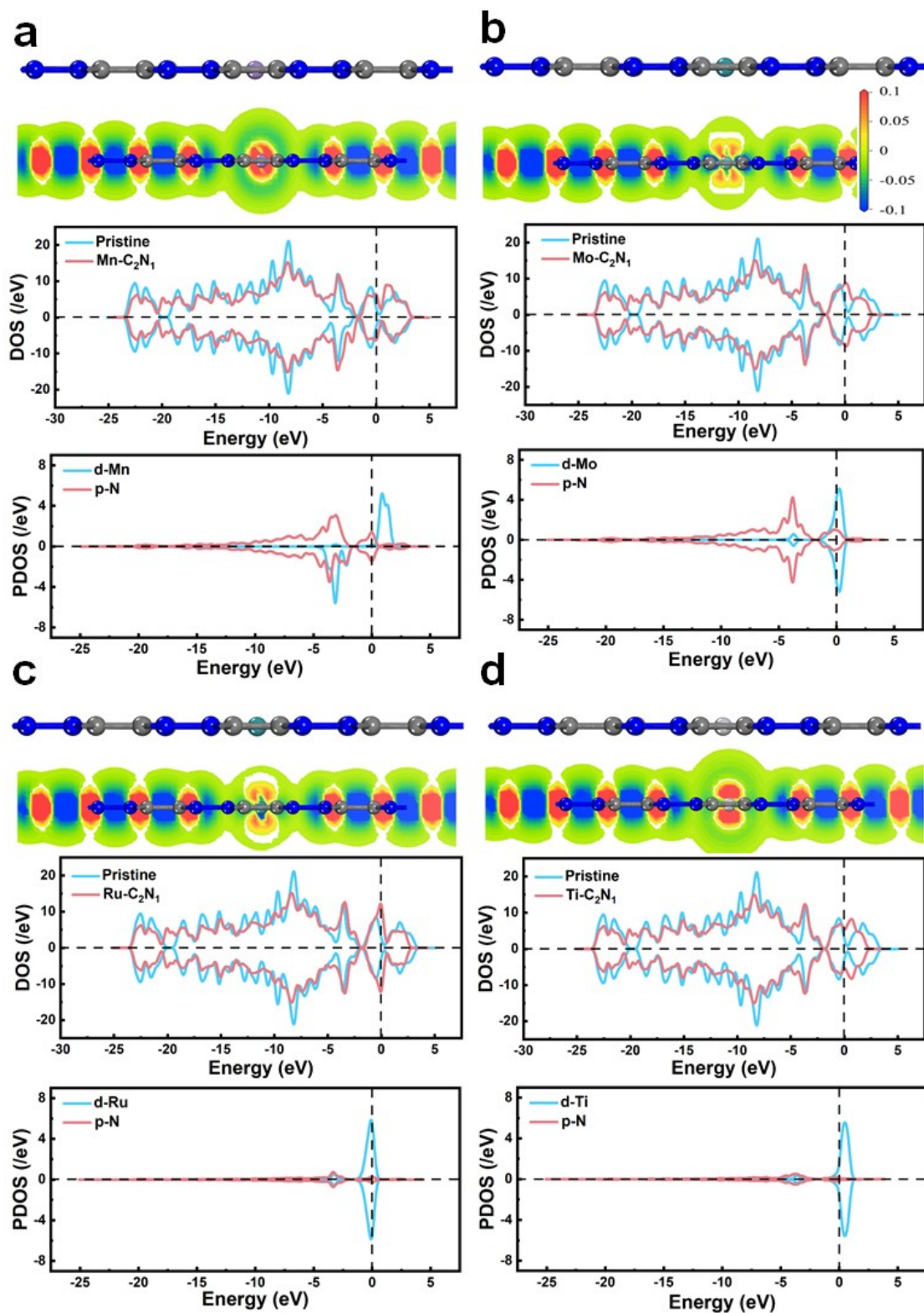
Figure S5. Density of states and charge density of 1TM-C_2N_1 (a) Mn-C_2N_1, (b) Mo-C_2N_1. (c) Ru-C_2N_1, and (d) Ti-C_2N_1. Densities are displayed with an isosurface and the interval of isovalue is between −0.1 and 0.1 e/Å^3.
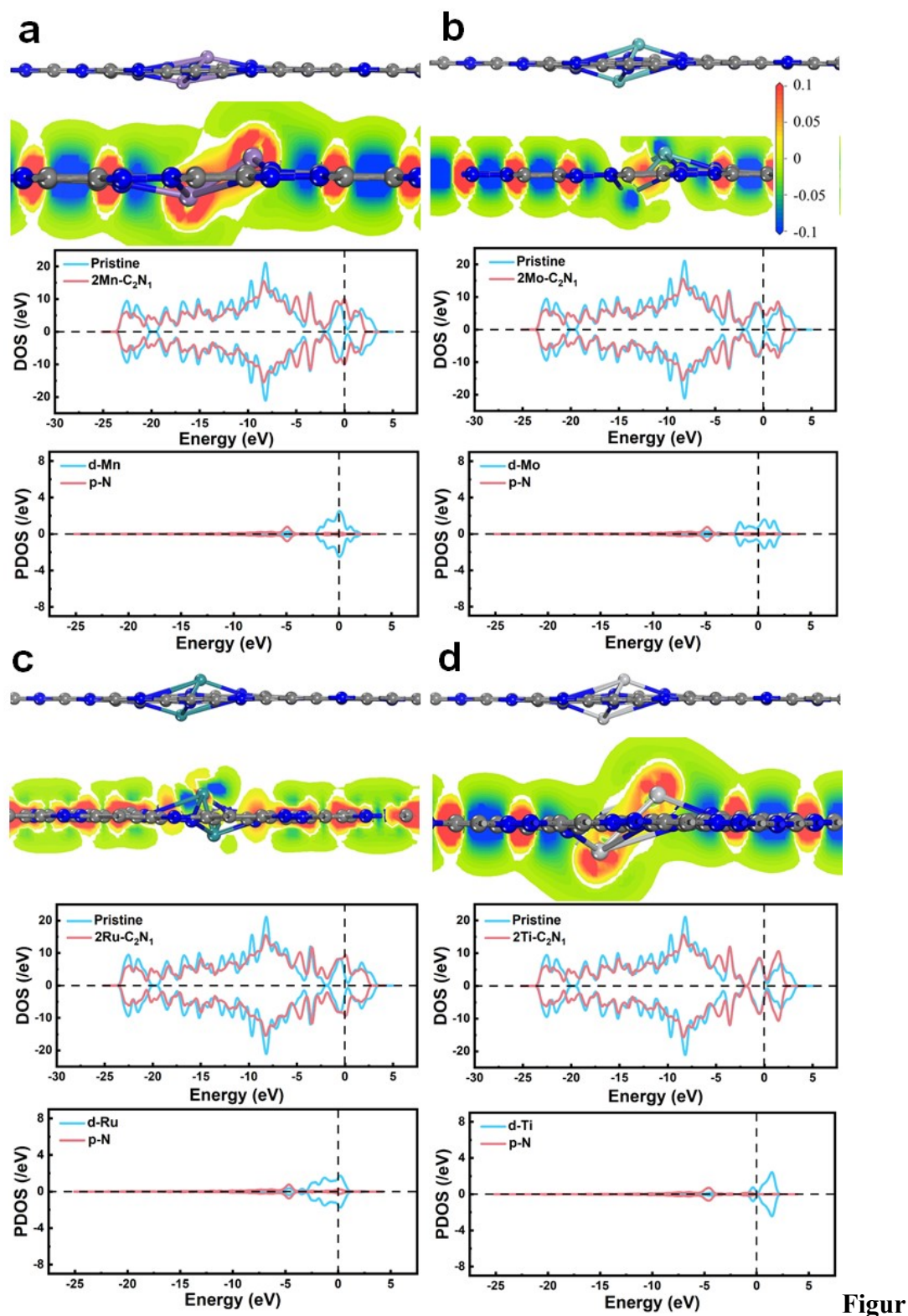
Figure S6. Density of states and charge density of 2TM-C_2N_1 (a) 2Mn-C_2N_1, (b) 2Mo-C_2N_1. (c) 2Ru-C_2N_1, and (d) 2Ti-C_2N_1. Densities are displayed with an isosurface and the interval of isovalue is between −0.1 and 0.1 e/Å^3.

Figure S7. Density of states and charge density of 3TM-C_2N_1 (a) 3Mn-C_2N_1, (b) 3Mo-C_2N_1. (c) 3Ru-C_2N_1, and (d) 3Ti-C_2N_1. Densities are displayed with an isosurface and the interval of isovalue is between −0.1 and 0.1 e/$Å^3$.
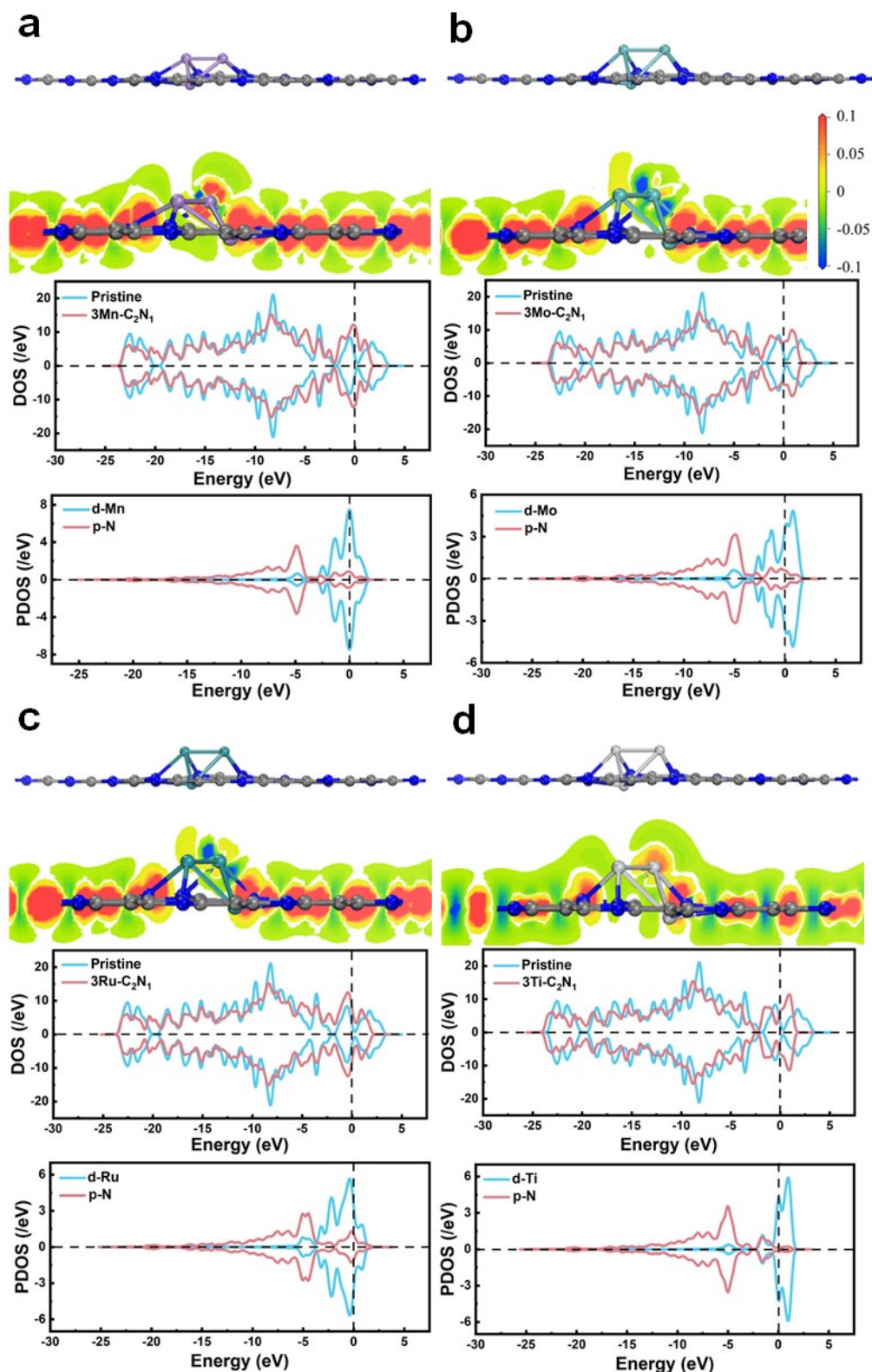
Figure S8. Density of states and charge density of 4TM-C_2N_1 (a) 4Mn-C_2N_1, (b) 4Mo-C_2N_1. (c) 4Ru-C_2N_1, and (d) 4Ti-C_2N_1. Densities are displayed with an isosurface and the interval of isovalue is between −0.1 and 0.1 e/$Å^3$.

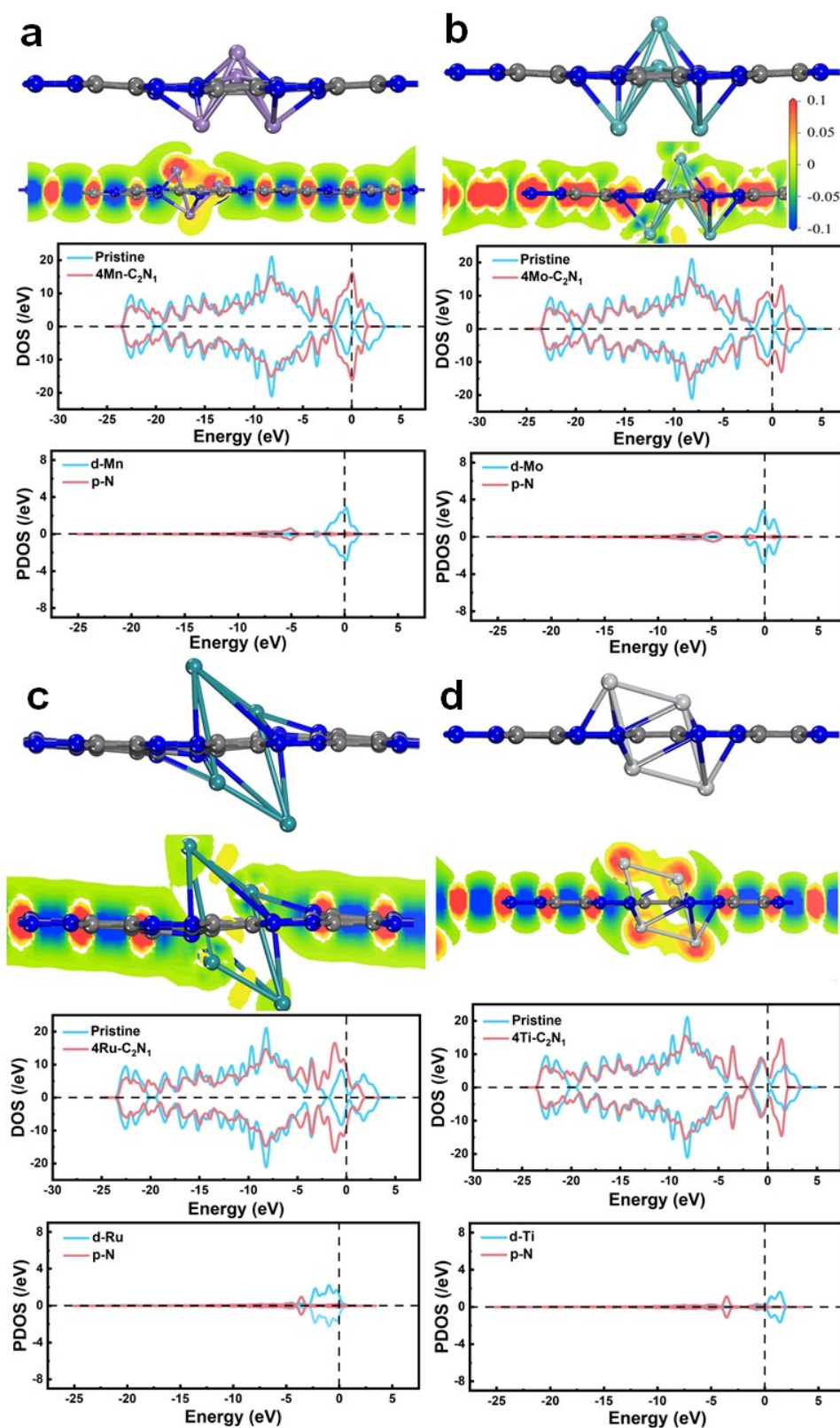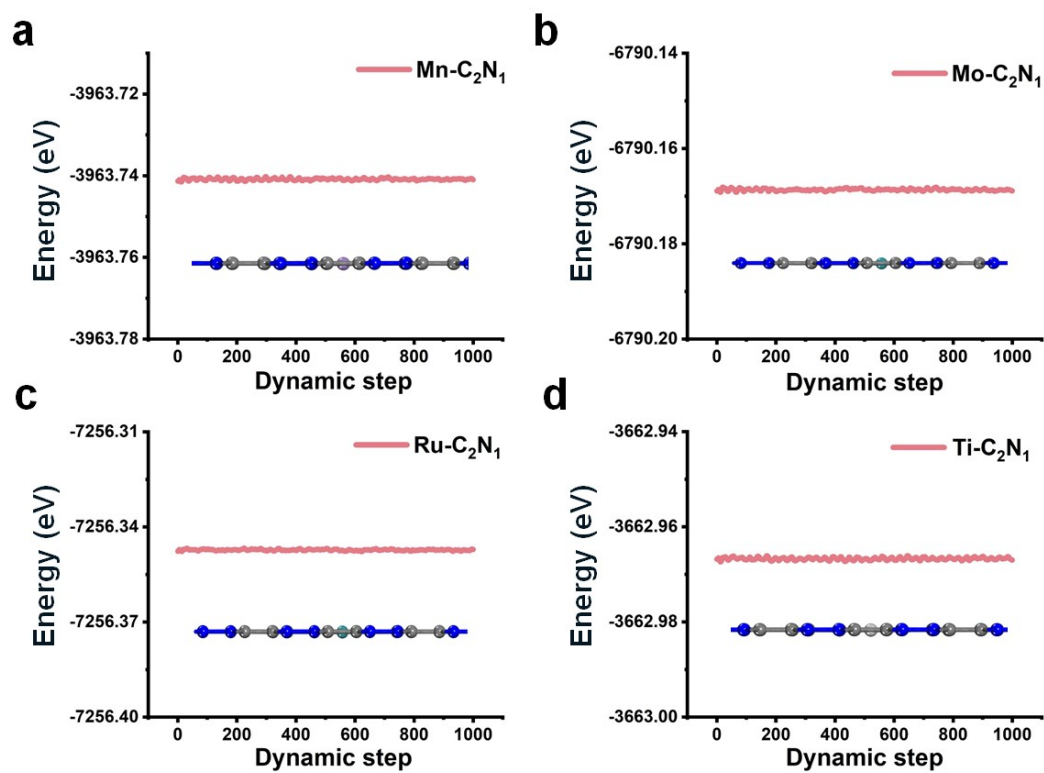**Figure S9**. The *ab initio* molecular dynamics of CO_2 on (a) Mn-C_2N_1, (b) Mo-C_2N_1, (c) Ru-C_2N_1 and (d) Ti-C_2N_1 monolayer.
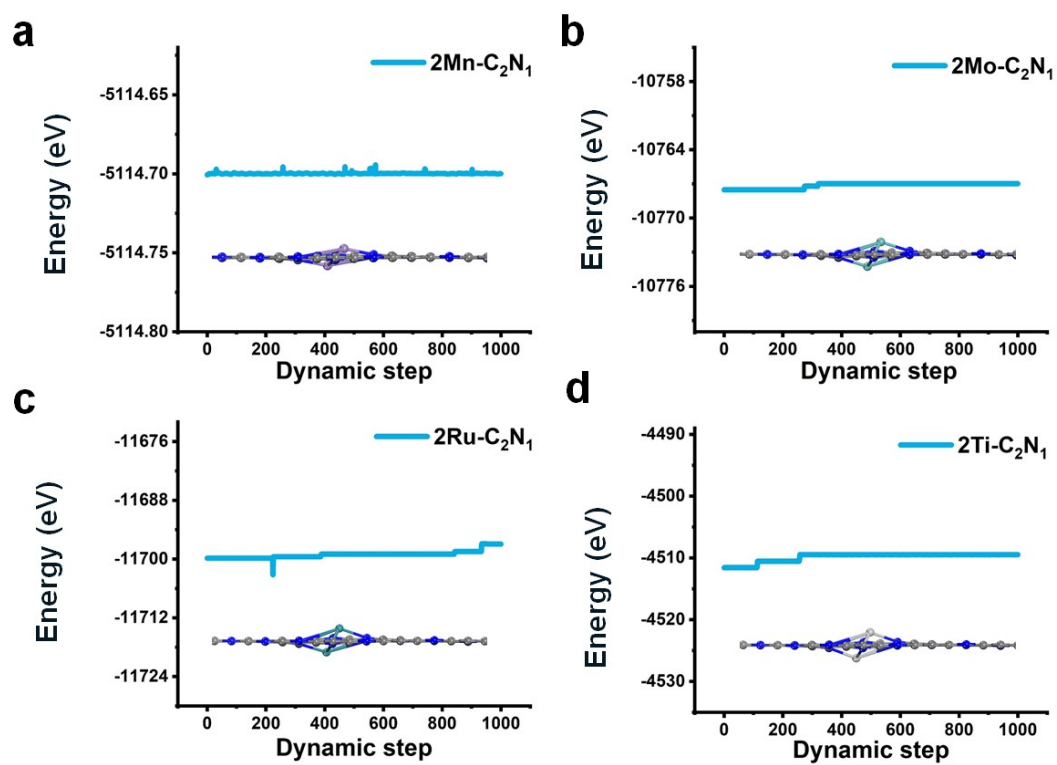
Figure S10. The *ab initio* molecular dynamics of CO_2 on (a) 2Mn-C_2N_1, (b) 2Mo-C_2N_1, (c) 2Ru-C_2N_1 and (d) 2Ti-C_2N_1 monolayer.
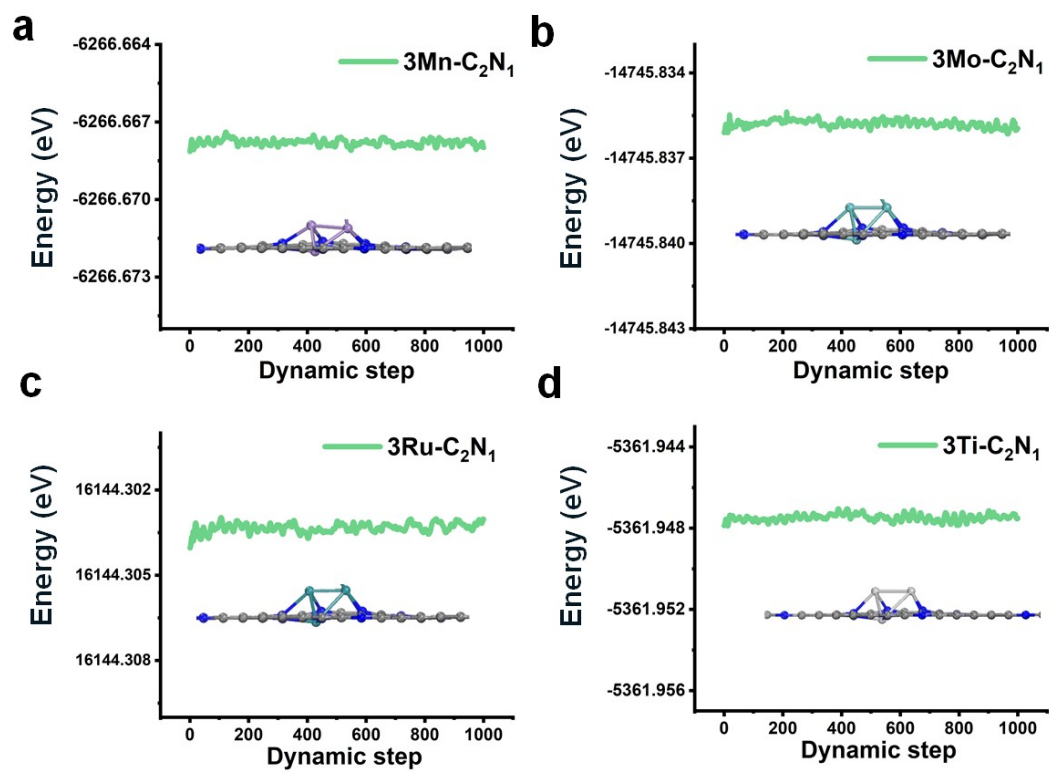
Figure S11. The *ab initio* molecular dynamics of CO_2 on (a) 3Mn-C_2N_1, (b) 3Mo-C_2N_1, (c) 3Ru-C_2N_1 and (d) 3Ti-C_2N_1 monolayer.

a

4Mn-C$_2$N$_1$

Energy (eV)

-7416.78
-7416.81
-7416.84
-7416.87

0 200 400 600 800 1000
Dynamic step

b

4Mo-C$_2$N$_1$

Energy (eV)

-18721.8
-18722.0
-18722.2
-18722.4

0 200 400 600 800 1000
Dynamic step

c

4Ru-C$_2$N$_1$

Energy (eV)

-20586.90
-20586.92
-20586.94
-20586.96

0 200 400 600 800 1000
Dynamic step

d

4Ti-C$_2$N$_1$

Energy (eV)

-6210.1
-6210.2
-6210.3
-6210.4
-6210.5

0 200 400 600 800 1000
Dynamic step
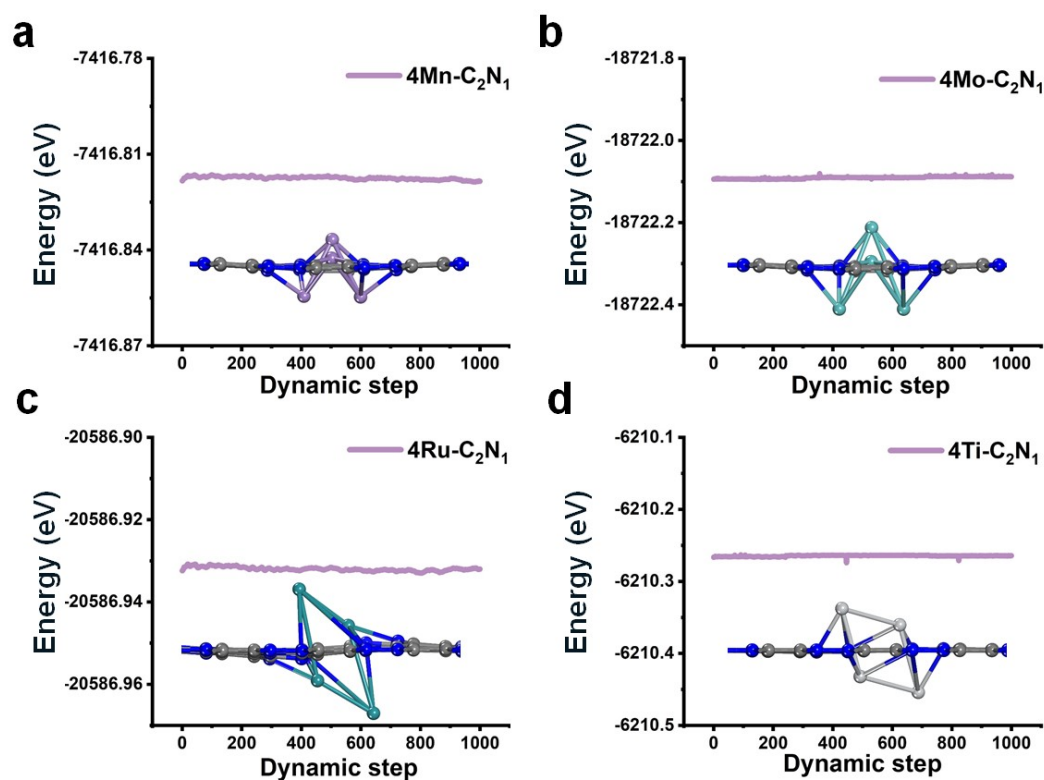
Figure S12. The *ab initio* molecular dynamics of CO$_2$ on (a) 4Mn-C$_2$N$_1$, (b) 4Mo-C$_2$N$_1$, (c) 4Ru-C$_2$N$_1$ and (d) 4Ti-C$_2$N$_1$ monolayer.
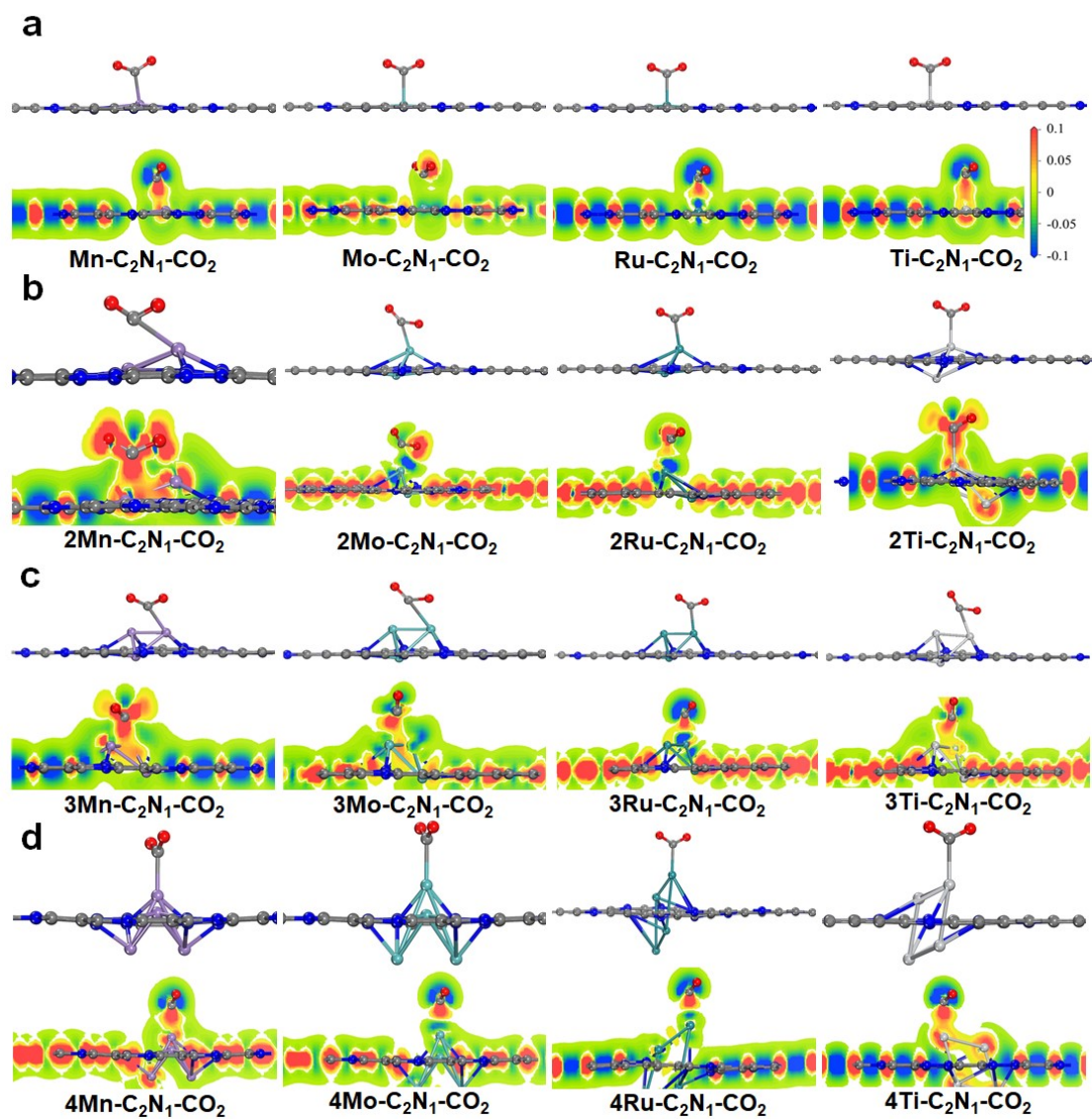
Figure S13. Charge density of CO_2 on TM-C_2N_1. (a) 1TM-C_2N_1-CO_2, (b) 2TM-C_2N_1-CO_2. (c) 3TM-C_2N_1-CO_2, and (d) 4TM-C_2N_1-CO_2. Densities are displayed with an isosurface and the interval of isovalue is between −0.1 and 0.1 e/$Å^3$.
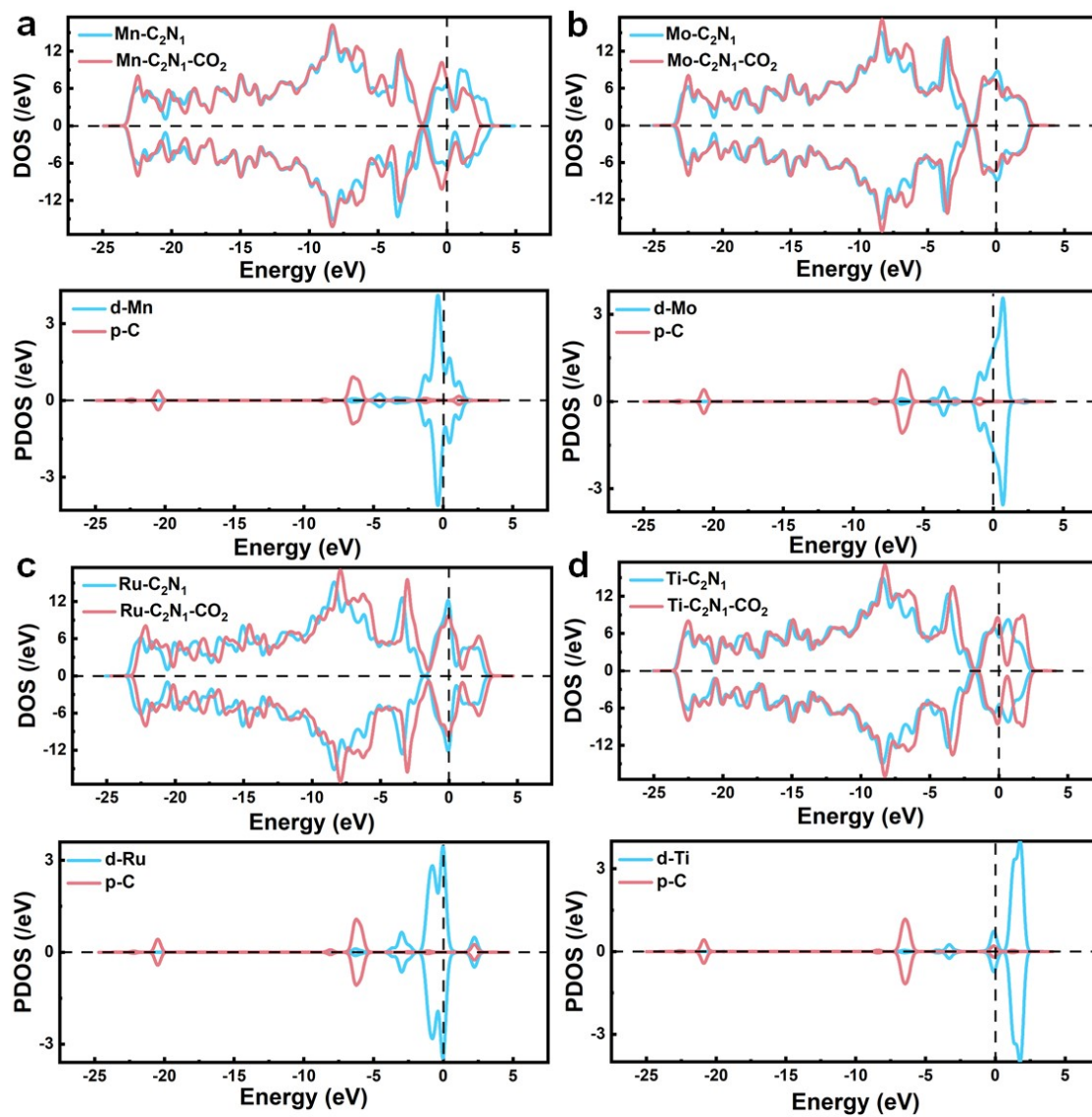
Figure S14. Density of states of (a) $Mn-C_2N_1-CO_2$, (b) $Mo-C_2N_1-CO_2$. (c) $Ru-C_2N_1-CO_2$, and (d) $Ti-C_2N_1-CO_2$.
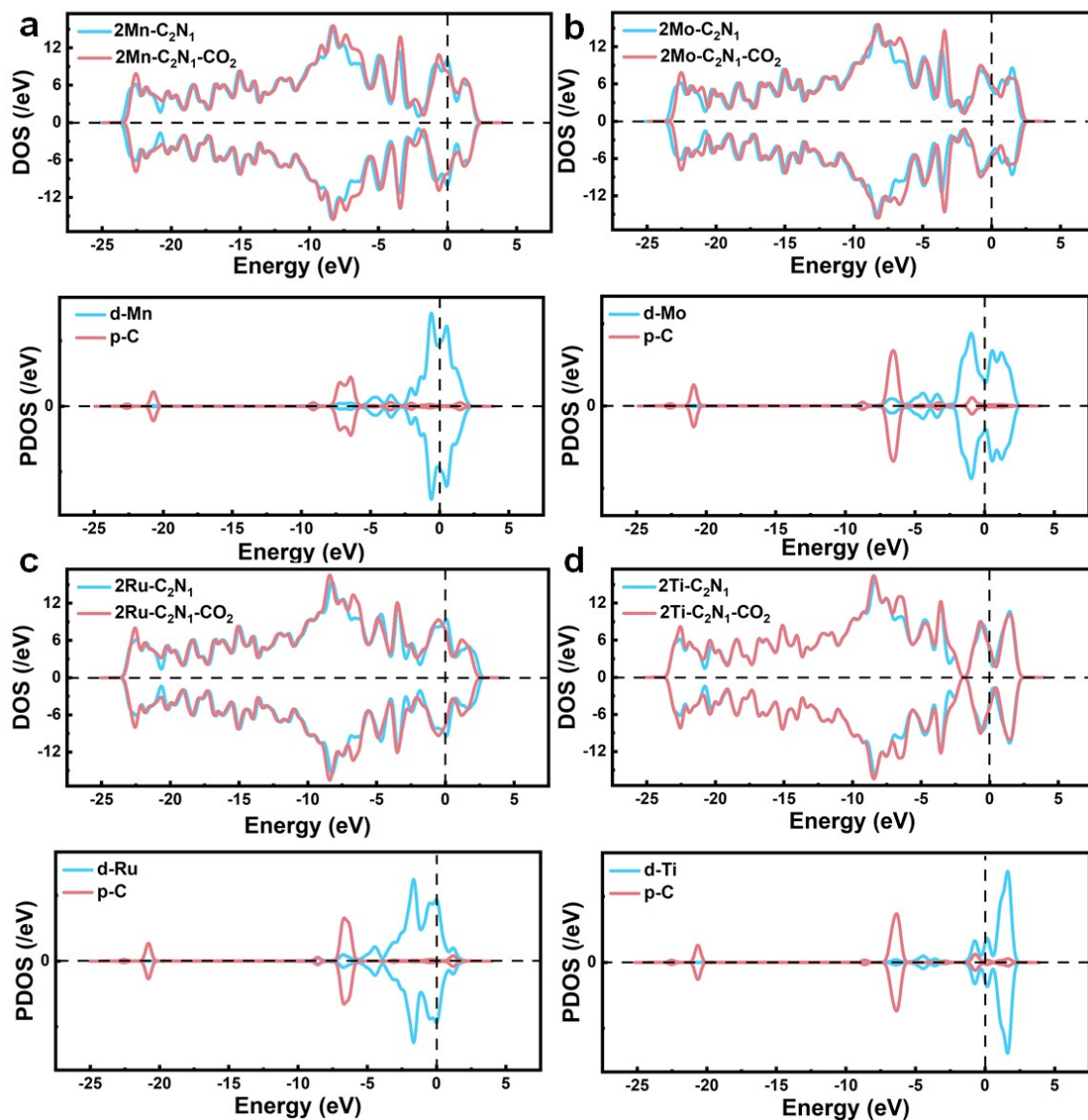
Figure S15. Density of states of (a) $2Mn-C_2N_1-CO_2$, (b) $2Mo-C_2N_1-CO_2$. (c) $2Ru-C_2N_1-CO_2$, and (d) $2Ti-C_2N_1-CO_2$.
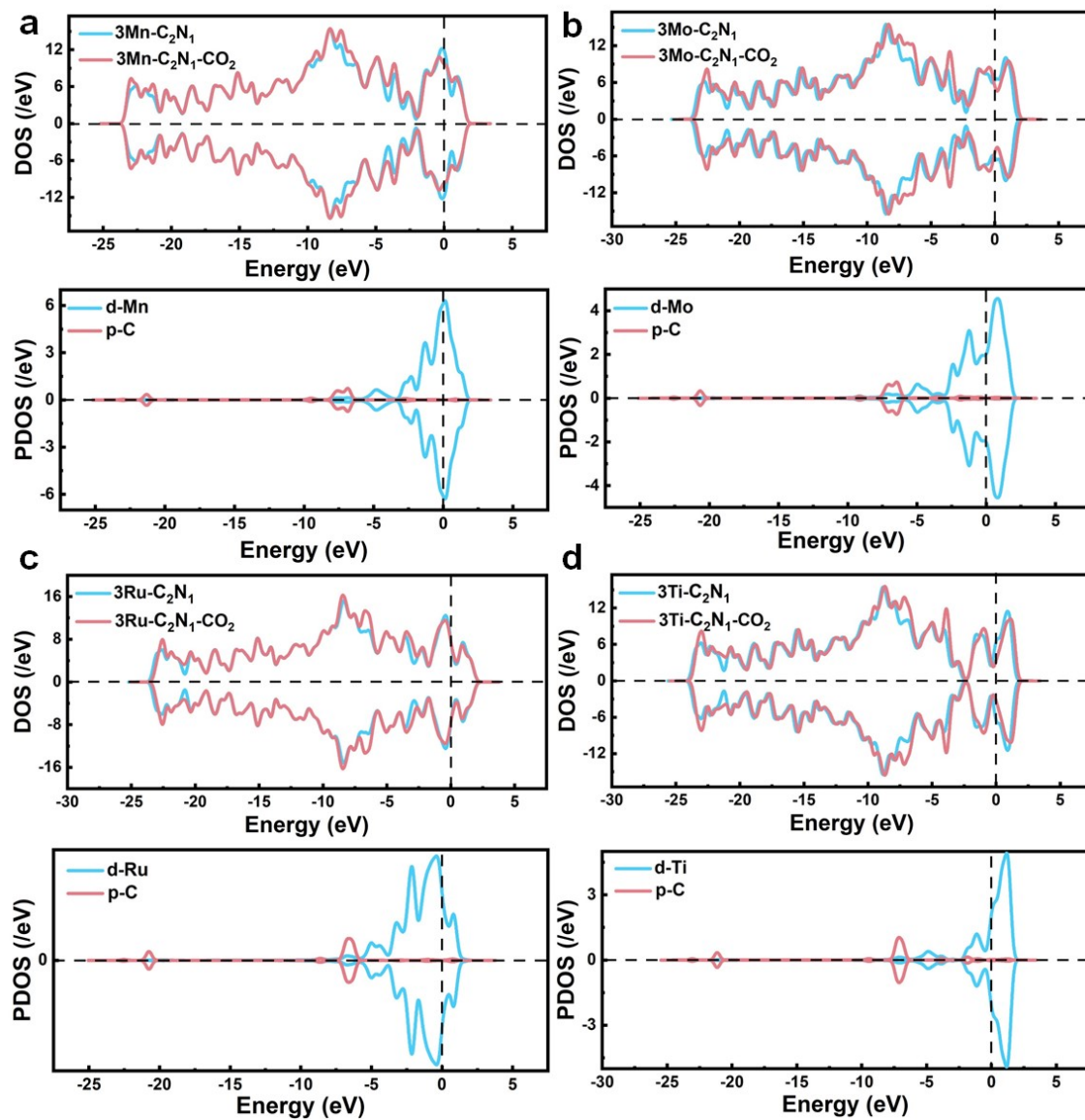
Figure S16. Density of states of (a) $3Mn-C_2N_1-CO_2$, (b) $3Mo-C_2N_1-CO_2$. (c) $3Ru-C_2N_1-CO_2$, and (d) $3Ti-C_2N_1-CO_2$.
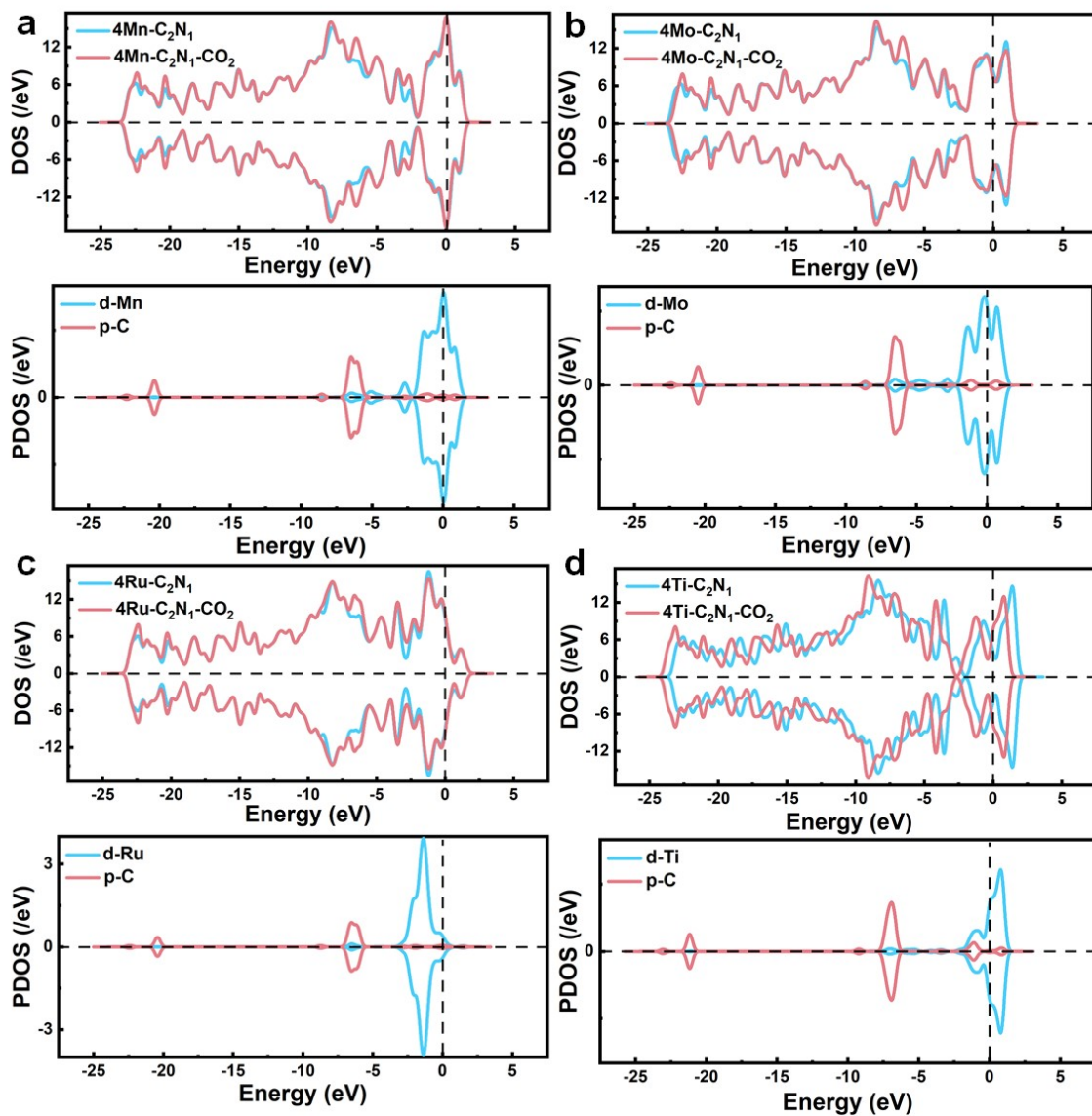
Figure S17. Density of states of (a) $4Mn-C_2N_1-CO_2$, (b) $4Mo-C_2N_1-CO_2$. (c) $4Ru-C_2N_1-CO_2$, and (d) $4Ti-C_2N_1-CO_2$.
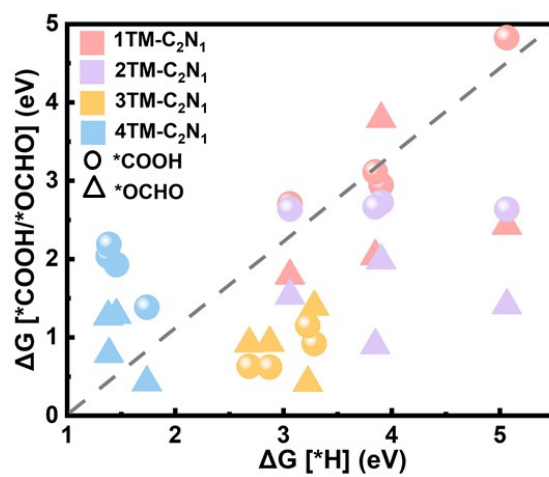
Figure S18. Free energy change of the first protonation step in the CO$_2$RR and HER.

Figure S19. The initial and the final stable configurations of CO_2 on the 1TM-C_2N_1.
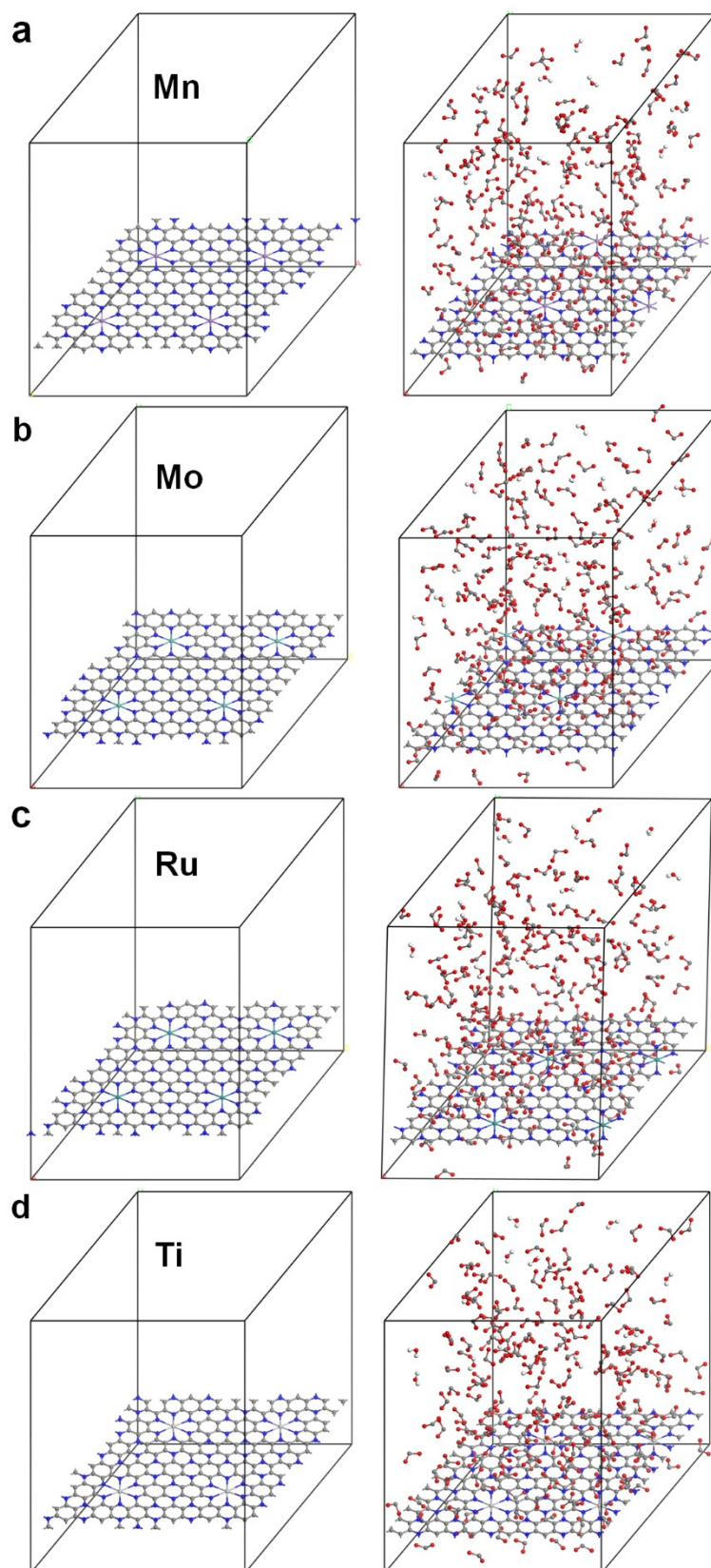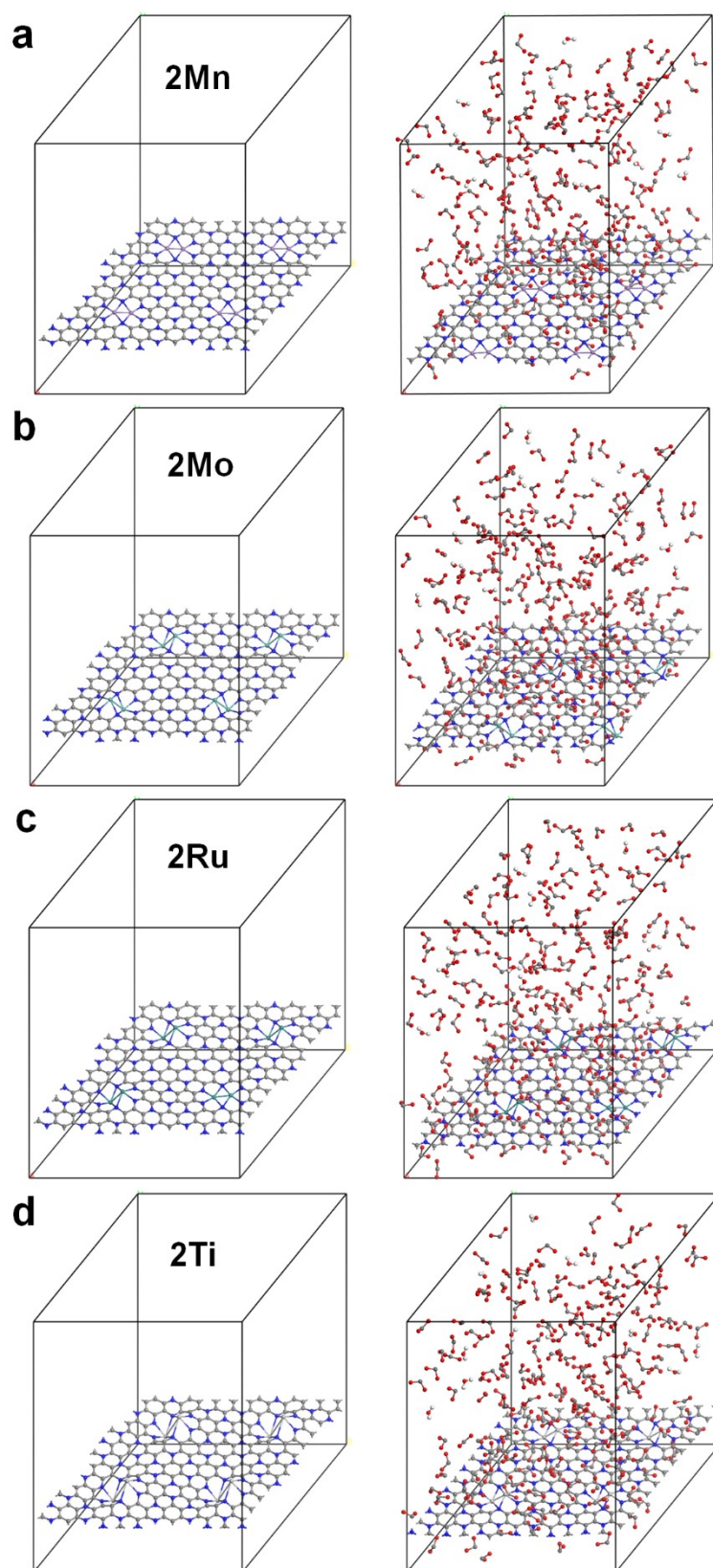
Figure S20. The initial and the final stable configurations of CO_2 on the 2TM-C_2N_1.
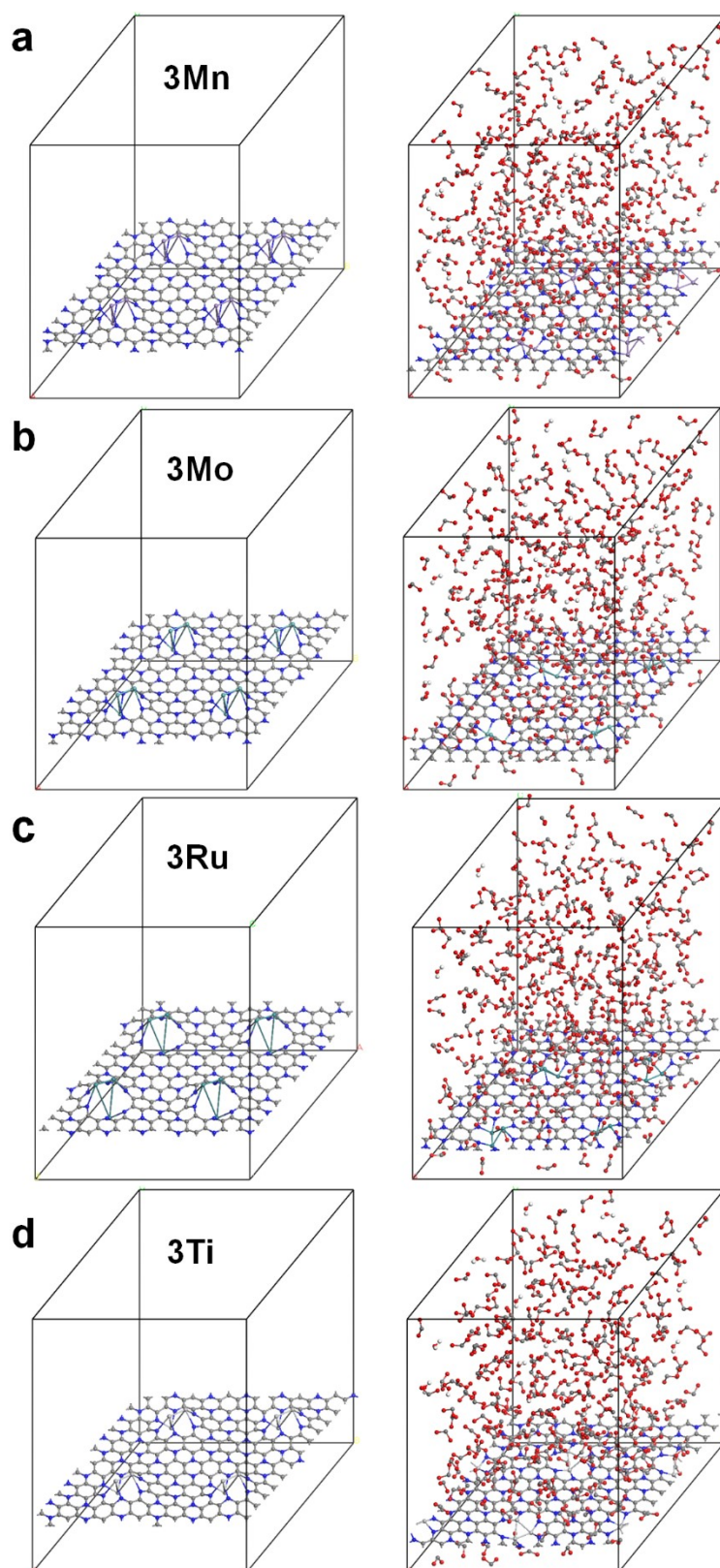
Figure S21. The initial and the final stable configurations of CO_2 on the 3TM-C_2N_1.

a 4Mn

b 4Mo

c 4Ru

d 4Ti
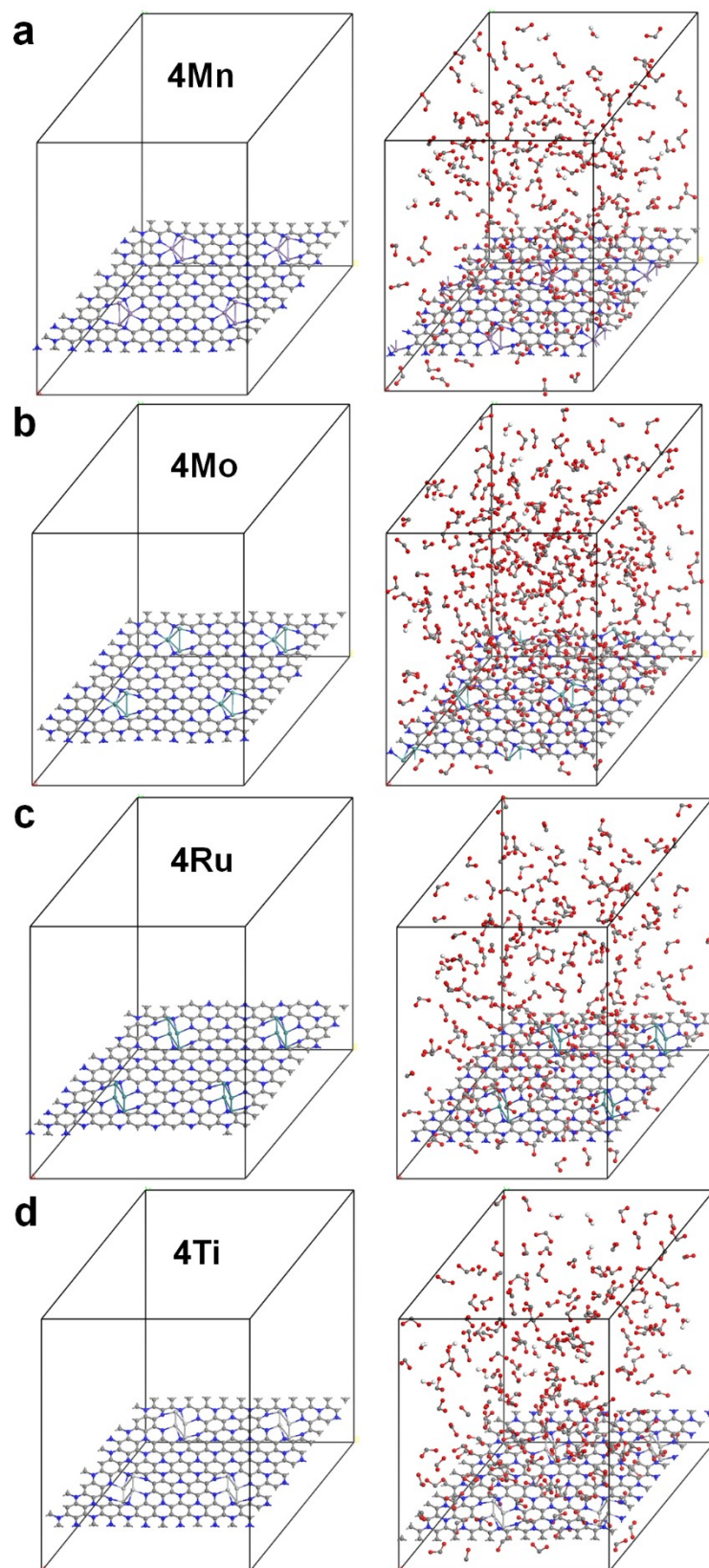
Figure S22. The initial and the final stable configurations of CO_2 on the 4TM-C_2N_1.
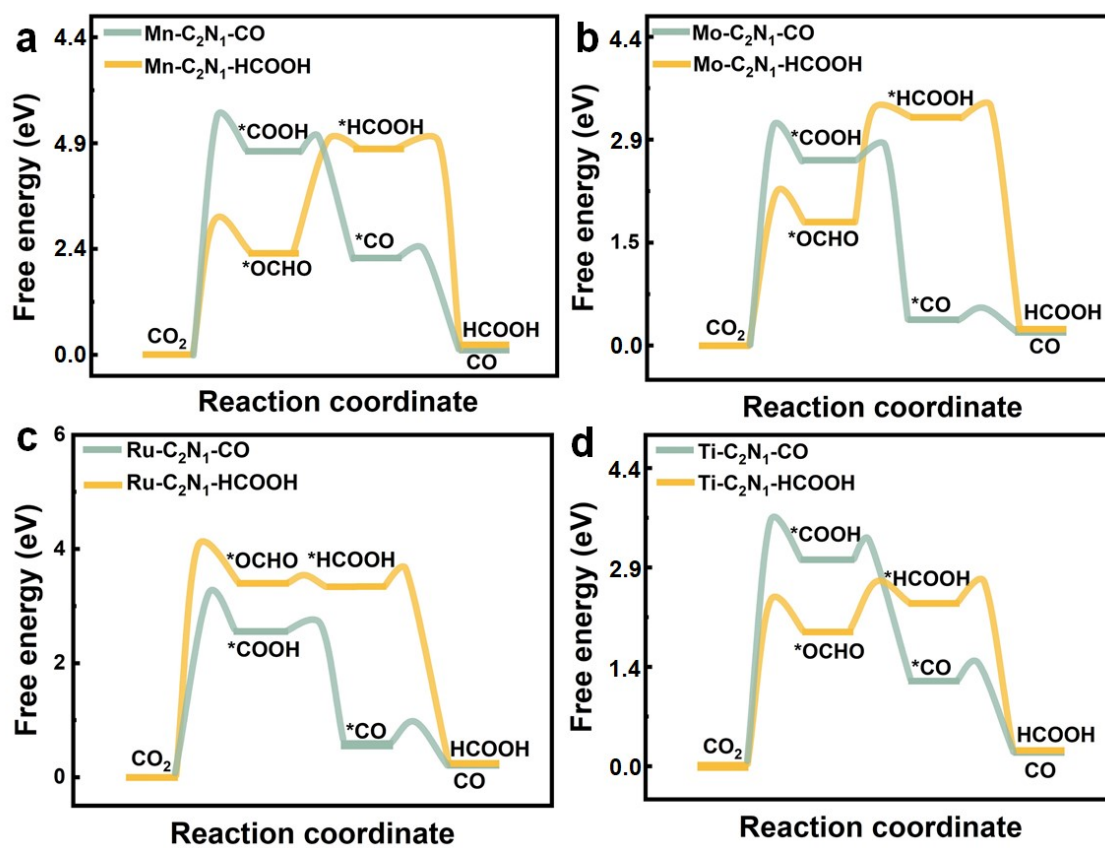
Figure S23. Gibbs free energy distribution diagram of CO_2 reduction pathway toward CO or HCOOH on (a) Mn-C_2N_1, (b) Mo-C_2N_1. (c) Ru-C_2N_1, and (d) Ti-C_2N_1.
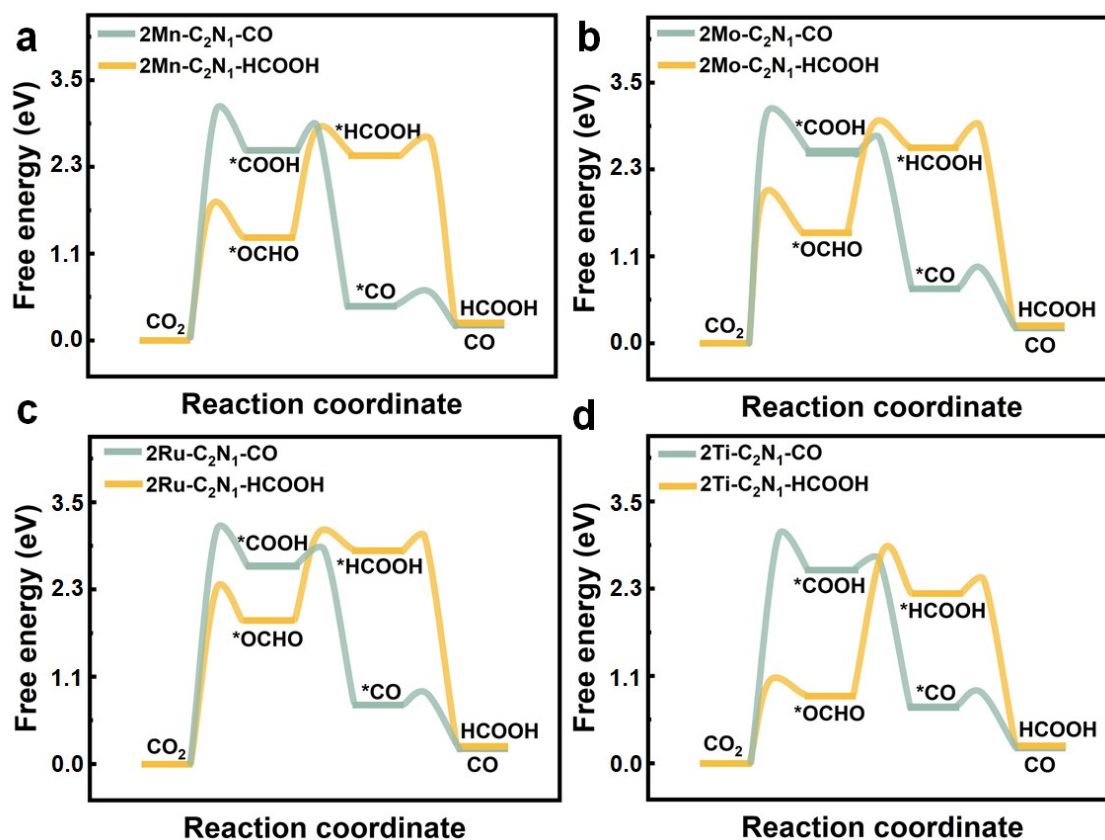
Figure S24. Gibbs free energy distribution diagram of CO_2 reduction pathway toward CO or HCOOH on (a) 2Mn-C_2N_1, (b) 2Mo-C_2N_1. (c) 2Ru-C_2N_1, and (d) 2Ti-C_2N_1.
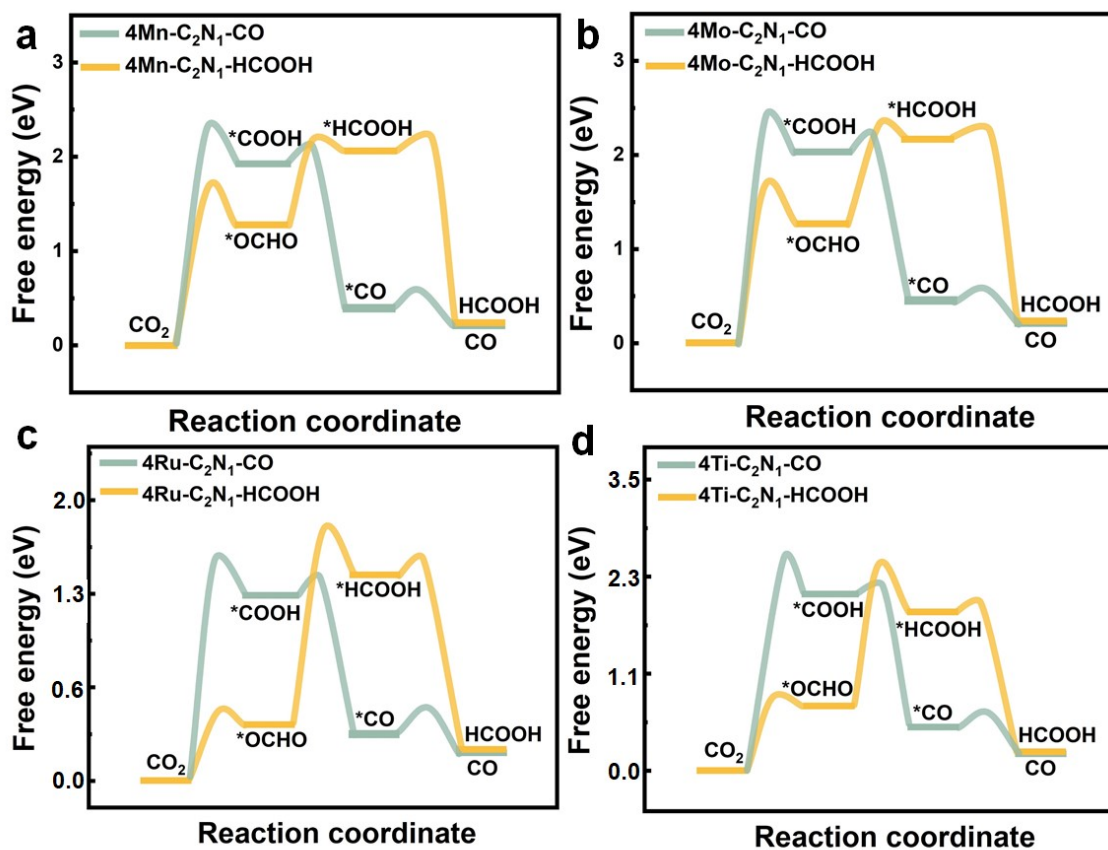
Figure S25. Gibbs free energy distribution diagram of CO_2 reduction pathway toward CO or HCOOH on (a) $4Mn\text{-}C_2N_1$, (b) $4Mo\text{-}C_2N_1$. (c) $4Ru\text{-}C_2N_1$, and (d) $4Ti\text{-}C_2N_1$.
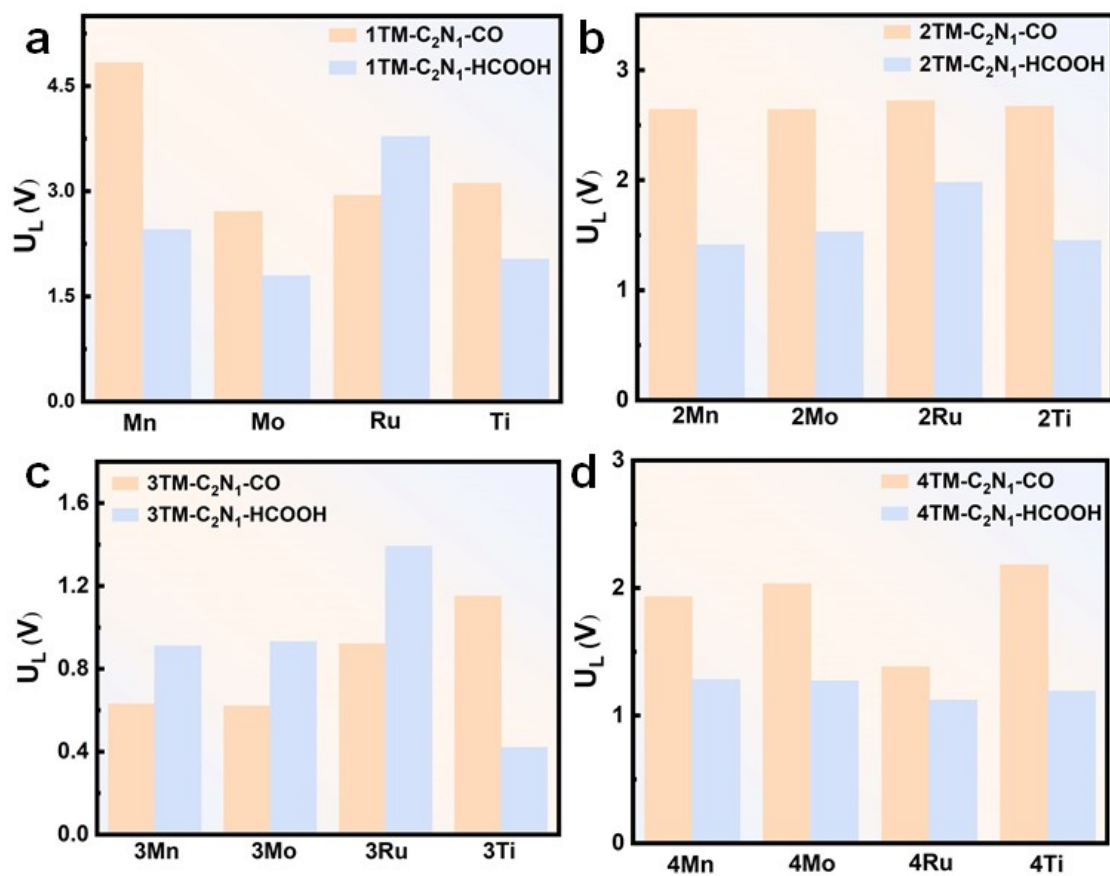
Figure S26. The limiting potential of CO or HCOOH on TM-C_2N_1. (a) 1TM-C_2N_1, (b) 2TM-C_2N_1. (c) 3TM-C_2N_1, and (d) 4TM-C_2N_1.
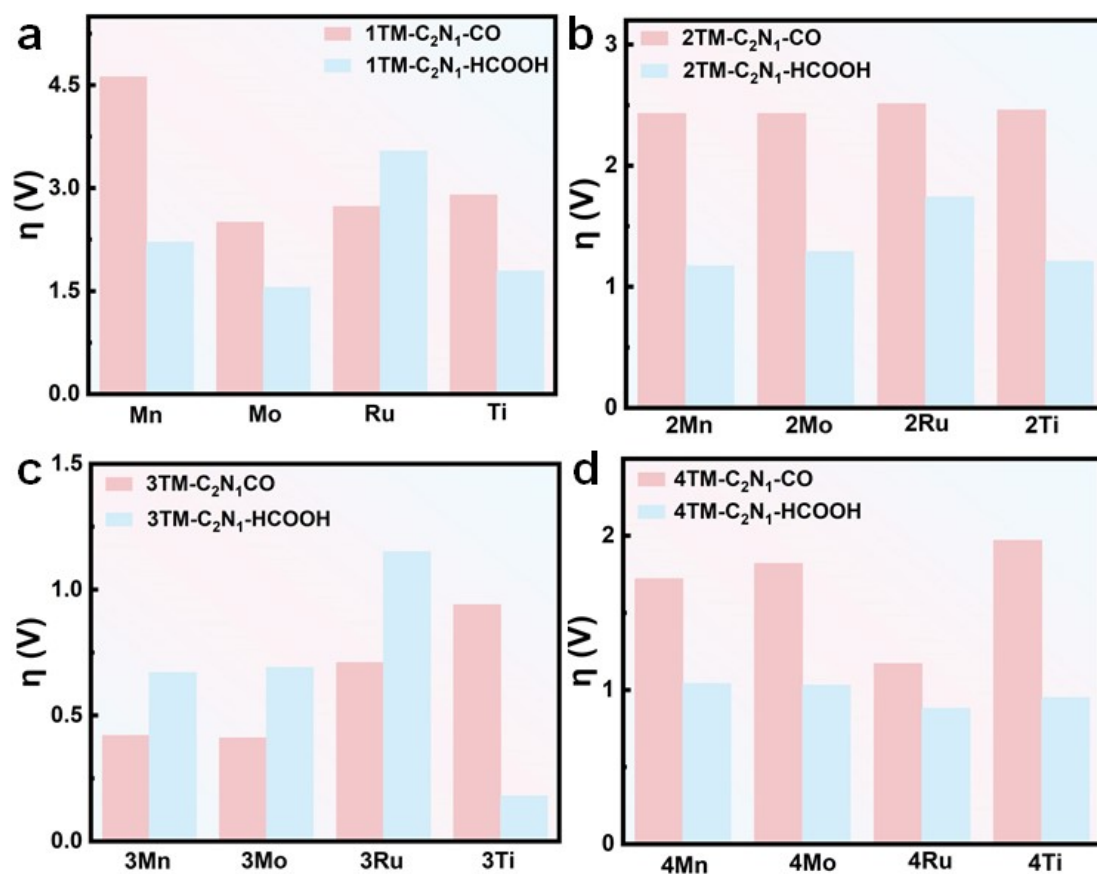
Figure S27. Overpotential of CO or HCOOH on TM-C_2N_1. (a) 1TM-C_2N_1, (b) 2TM-C_2N_1. (c) 3TM-C_2N_1, and (d) 4TM-C_2N_1.
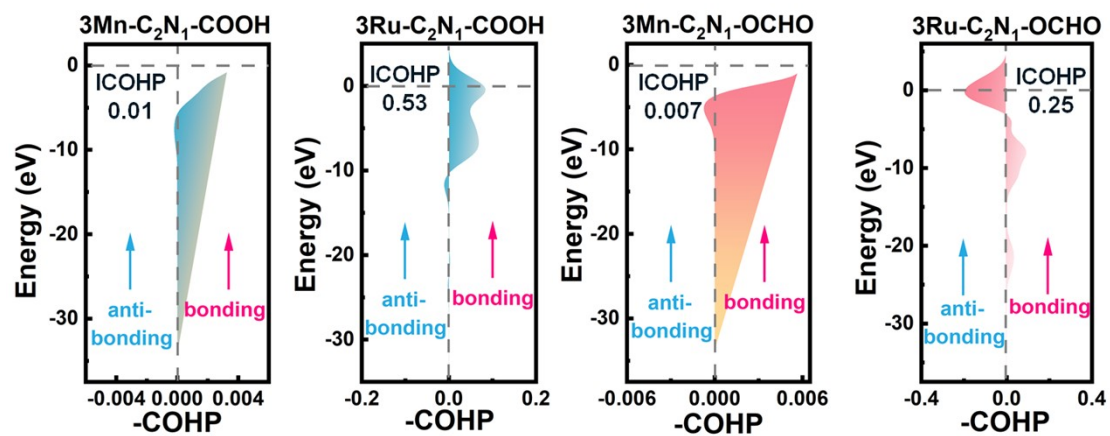
Figure S28. ICOHP value of *COOH and *OCHO on the 3TM-C_2N_1.
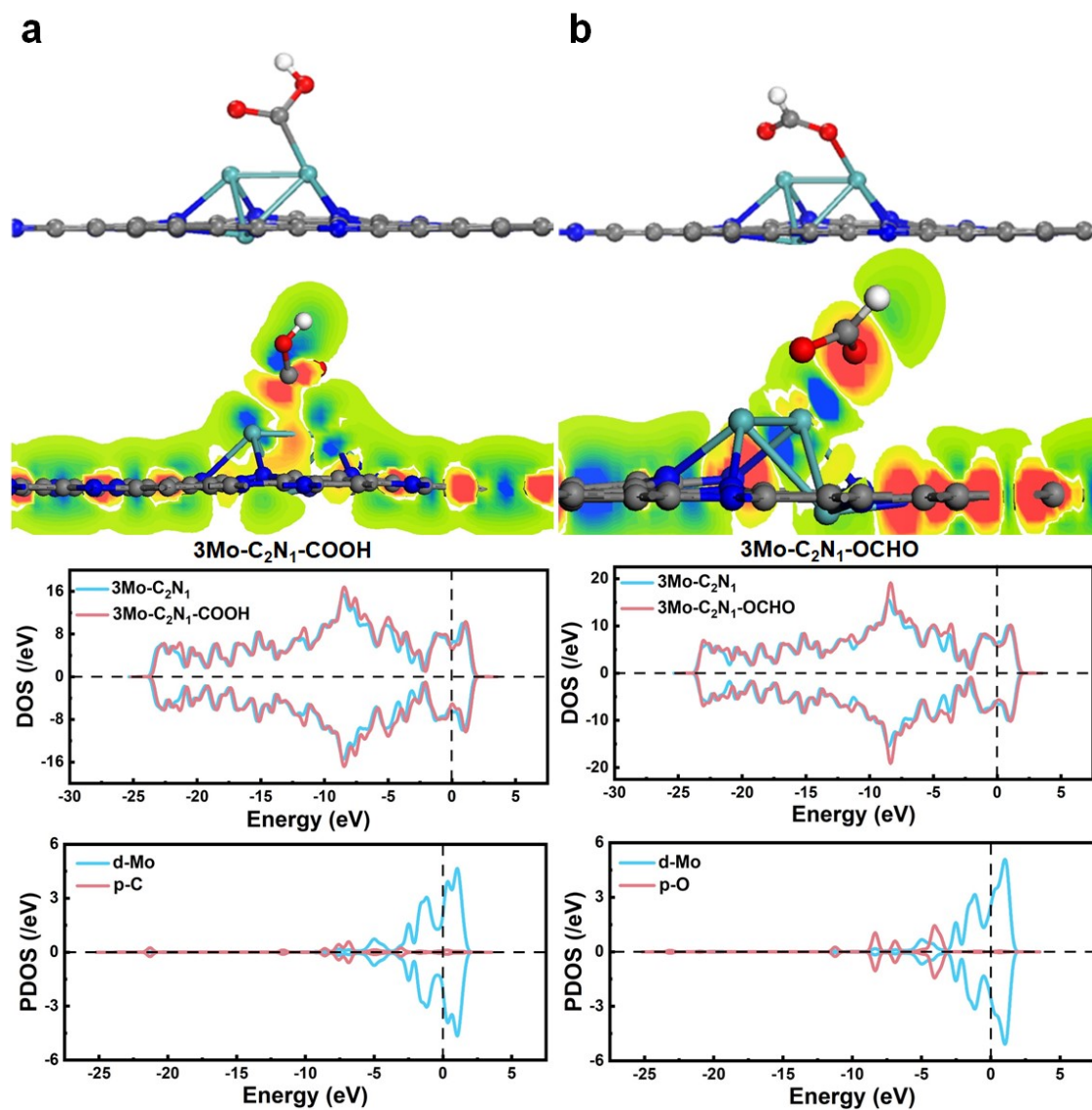
Figure S29. The stable structure, charge density, and DOS of (a) *COOH and (b) *OCHO on 3Mo-C_2N_1. Densities are displayed with an isosurface and the interval of isovalue is between −0.1 and 0.1 e/Å^3.

a

b

3Ti-C$_2$N$_1$-COOH
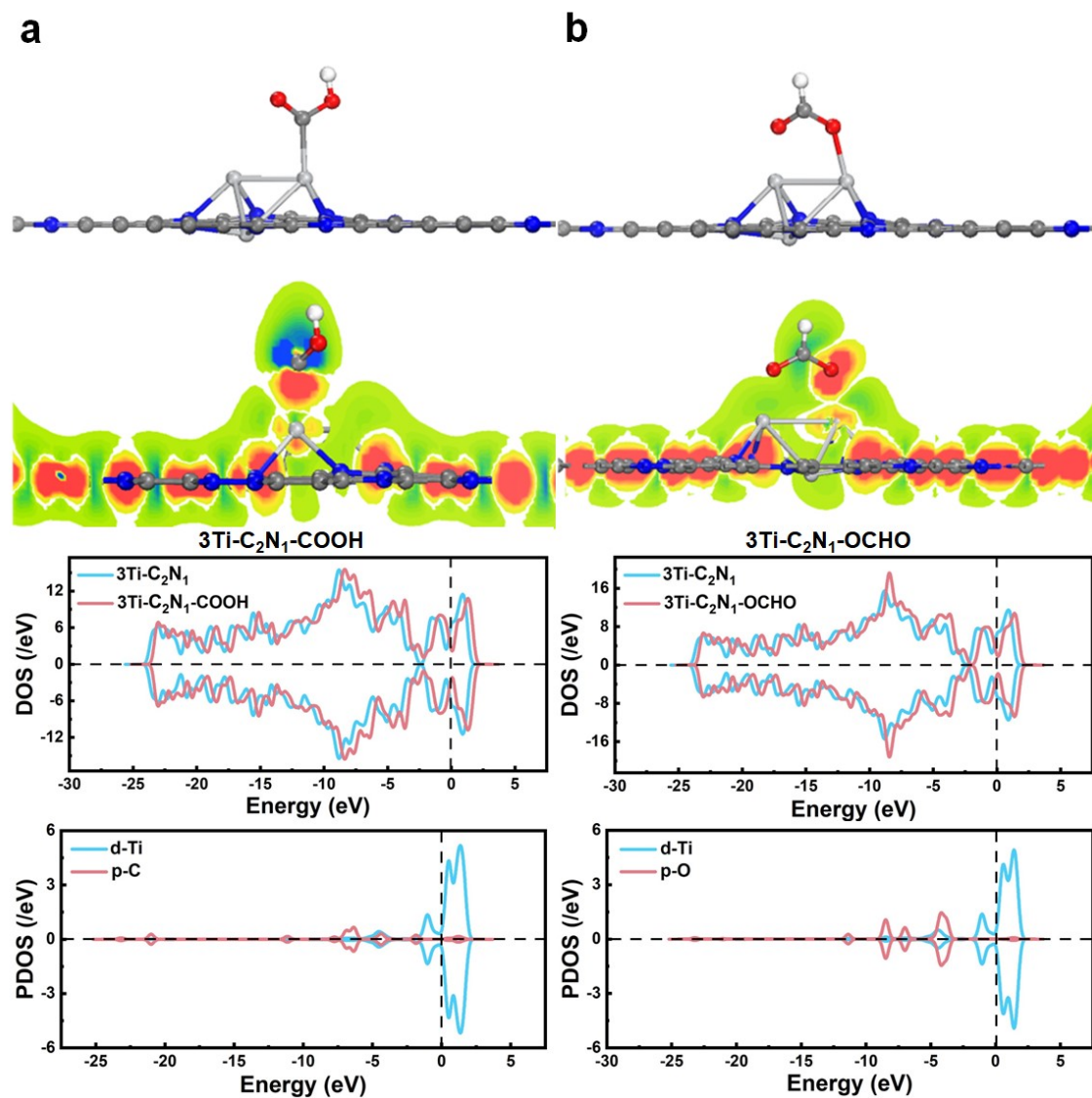
3Ti-C$_2$N$_1$-OCHO

Figure S30. The stable structure, charge density, and DOS of (a) *OCHO and (b) *COOH on 3Ti-C$_2$N$_1$. Densities are displayed with an isosurface and the interval of isovalue is between −0.1 and 0.1 e/Å^3.

Table S1. The adsorption energies (E_{ads}), bond lengths of C and O atoms in CO_2 (d_{c-o}), O-C-O angles of the most stable CO_2 adsorption configurations on the TM-C_2N_1.

| Models	E_{ads} (eV)	d_{c-o} (A)	O-C-O angles
Mn-C_2N_1	-2.60	1.20/1.18	163.22
Mo-C_2N_1	-0.29	1.21/1.21	152.58
Ru-C_2N_1	-0.29	1.20/1.20	157.20
Ti-C_2N_1	-0.53	1.19/1.23	152.90
2Mn-C_2N_1	-1.50	1.24/1.32	137.32
2Mo-C_2N_1	-1.16	1.23/1.29	134.92
2Ru-C_2N_1	-0.88	1.24/1.26	136.58
2Ti-C_2N_1	-1.13	1.22/1.28	138.267
3Mn-C_2N_1	-1.76	1.28/1.28	133.43
3Mo-C_2N_1	-1.56	1.25/1.32	127.32
3Ru-C_2N_1	-0.94	1.24/1.26	135.28
3Ti-C_2N_1	-1.51	1.23/1.32	127.19
4Mn-C_2N_1	-1.61	1.28/1.27	134.52
4Mo-C_2N_1	-1.47	1.27/1.27	129.91
4Ru-C_2N_1	-2.14	1.28/1.28	136.79
4Ti-C_2N_1	-1.44	1.27/1.27	130.92

Table S2. The adsorption energy E_{ads} (eV) of H_2O on the TM-C_2N_1.

Models	E_{ads} (eV)
Mn-C_2N_1	-0.95
Mo-C_2N_1	-0.80
Ru-C_2N_1	-0.57
Ti-C_2N_1	-1.03
2Mn-C_2N_1	-0.84
2Mo-C_2N_1	-0.96
2Ru-C_2N_1	-0.67
2Ti-C_2N_1	-0.96
3Mn-C_2N_1	-0.93
3Mo-C_2N_1	-0.90
3Ru-C_2N_1	-0.74
3Ti-C_2N_1	-1.10
4Mn-C_2N_1	-1.13
4Mo-C_2N_1	-1.02
4Ru-C_2N_1	-0.97
4Ti-C_2N_1	-1.17

Table S3. Diffusion coefficient of CO_2 on the TM-C_2N_1

Models	CO_2
Mn-C_2N_1	4.15
Mo-C_2N_1	4.52
Ru-C_2N_1	4.27
Ti-C_2N_1	4.95
2Mn-C_2N_1	3.87
2Mo-C_2N_1	5.33
2Ru-C_2N_1	4.24
2Ti-C_2N_1	4.22
3Mn-C_2N_1	2.91
3Mo-C_2N_1	2.19
3Ru-C_2N_1	3.86
3Ti-C_2N_1	2.78
4Mn-C_2N_1	3.73
4Mo-C_2N_1	3.89
4Ru-C_2N_1	3.74
4Ti-C_2N_1	4.24

References

[1] B. Delley, From molecules to solids with the DMol^3 approach, The Journal of Chemical Physics, 113 (2000) 7756-7764.

[2] S. Zhuo, Y. Huang, J. Hu, H. Liu, Y. Hu, J. Jiang, Computer Simulation for Adsorption of CO_2, N_2 and Flue Gas in a Mimetic MCM-41, The Journal of Physical Chemistry C, 112 (2008) 11295-11300.

[3] X. Li, T. Guo, L. Zhu, C. Ling, Q. Xue, W. Xing, Charge-modulated CO_2 capture of C_3N nanosheet: Insights from DFT calculations, Chemical Engineering Journal, 338 (2018) 92-98.

[4] A.A. Peterson, F. Abild-Pedersen, F. Studt, J. Rossmeisl, J.K. Nørskov, How copper catalyzes the electroreduction of carbon dioxide into hydrocarbon fuels, Energy & Environmental Science, 3 (2010) 1311.

[5] J.K. Nørskov, J. Rossmeisl, A. Logadottir, L. Lindqvist, J.R. Kitchin, T. Bligaard, H. Jónsson, Origin of the Overpotential for Oxygen Reduction at a Fuel-Cell Cathode, The Journal of Physical Chemistry B, 108 (2004) 17886-17892.

[6] H. Yu, D. Wang, Y. Li, G. Chen, X. Ma, Explainable molecular simulation and machine learning for carbon dioxide adsorption on magnesium oxide, Fuel, 357 (2024) 129725.

[7] L. Tao, D. Dastan, W. Wang, P. Poldorn, X. Meng, M. Wu, H. Zhao, H. Zhang, L. Li, B. An, Metal-Decorated InN Monolayer Senses N_2 against CO_2, ACS Applied Materials & Interfaces, 15 (2023) 12534-12544.

[8] B. Mortazavi, I.S. Novikov, A.V. Shapeev, A machine-learning-based investigation on the mechanical/failure response and thermal conductivity of semiconducting BC_2N monolayers, Carbon, 188 (2022) 431-441.

[9] L. Tao, J. Huang, X. Yin, Q. Wang, Z. Li, G. Wang, B. Cui, Adsorption Kinetics of CO_2 on a Reconstructed Calcite Surface: An Experiment-Simulation Collaborative Method, Energy & Fuels, 33 (2019) 8946-8953.

[10] A. Einstein, On the movement of small particles suspended in stationary liquids required by the molecularkinetic theory of heat, Annalen der Physik, 322 (1905) 549-560.